



*Università Degli Studi di Milano-Bicocca*

Dipartimento di Fisica

Laboratorio di Misure Nucleari e Subnucleari I

## The Compton Scattering

*Filippo Lonti, Martina Mozzanica, Andrea Polesello*

Docenti  
Prof.ssa Chiara BROFFERIO  
Prof. Francesco TERRANOVA

Data  
09 giugno 2021

# Contents

<b>1</b>	<b>Theoretical Introduction</b>	<b>1</b>
1.1	Compton formula . . . . .	1
1.2	Klein-Nishina formula . . . . .	3
1.3	Positronium parity . . . . .	4
<b>2</b>	<b>Characterization</b>	<b>7</b>
2.1	Experimental setup . . . . .	8
2.1.1	Source . . . . .	8
2.1.2	Detectors . . . . .	9
2.1.3	Photomultipliers and Preamplifier . . . . .	10
2.1.4	Electronic Chain . . . . .	12
2.2	MCA linearity . . . . .	15
2.3	Resolution . . . . .	16
2.4	Shaping time . . . . .	18
2.5	Coincidence and autocoincidence . . . . .	21
2.6	Energy calibration . . . . .	24
2.7	Efficiency . . . . .	27
2.8	Temperature fluctuations and peak derive . . . . .	29
2.9	Geometrical setup . . . . .	31
2.10	Probability of interaction . . . . .	34
<b>3</b>	<b>Data analysis</b>	<b>39</b>
3.1	Background . . . . .	39
3.2	Compton Law . . . . .	40
3.3	Klein-Nishina differential cross section . . . . .	44
3.4	Parity of Positronium . . . . .	48
<b>4</b>	<b>Conclusion</b>	<b>53</b>
	<b>Appendices</b>	<b>54</b>
<b>A</b>	<b>Insights</b>	<b>55</b>
A.1	Detector 1-inch . . . . .	55
A.2	Detector 2-inch . . . . .	56

A.3	Smoothing . . . . .	58
A.4	Useful Tables . . . . .	60
A.5	Activity Table . . . . .	61
A.6	Rate estimation . . . . .	61
<b>B</b>	<b>Instrumentation List</b>	<b>64</b>
	<b>Bibliography</b>	<b>65</b>

# Chapter 1

## Theoretical Introduction

This experiment has the general goal of investigating the phenomenology of the Compton scattering, in particular by verifying the Compton Law and the Klein-Nishina formula for the differential cross section, using annihilation  $\gamma$  photons from a  $\beta^+$  source. The use of this tipology of source allowed to set a further goal for the experiment: the measurement of the parity of the positronium originated by the interaction of the emitted positron with an electron of the material.

### 1.1 Compton formula

Compton scattering is one of the three main processes through which electromagnetic radiation interacts with matter. In classical physics the scattering of a photon on a target electron is described as an elastic one, called Thomson scattering. In 1922 for the first time, Arthur Compton made  $X$  and  $\gamma$  photons incide on a graphite target, and he showed that the wavelength of the scattered photons was, in average, greater than the one of the incident photons: this interaction is indeed inelastic (Fig. 1.1). Thomson elastic scattering emerges as a limit of the Compton one for photons of  $E \ll m_e c^2$ , but doesn't hold for  $E \geq m_e c^2$ .

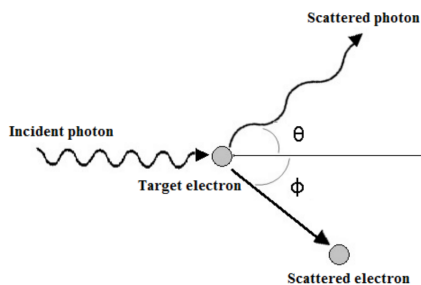


Figure 1.1: Compton scattering on free electron

An expression for the energy of the scattered photon can be easily obtained by imposing the conservation of momentum and energy: it's clear that the electron must recoil to ensure the conservation of momentum in the plane orthogonal to the direction of the incoming photon, and so obviously the energy of the photon must reduce after the interaction of a fraction depending only on the scattering angle. The result is known as Compton Law:

$$E' = h\nu' = \frac{h\nu}{1 - \frac{h\nu}{mc^2}(1 - \cos\theta)} \quad (1.1)$$

where  $\nu$  is the frequency of the incoming photon,  $\nu'$  is that of the outgoing one,  $\theta$  is the scattering angle and  $m$  is the electron mass. The proof of this formula is elementary. Working in the laboratory frame, the electron is at rest, so it can be described by a 4-vector  $p = (mc^2, 0, 0, 0)$ . Choosing the z-axis oriented as the trajectory of the incoming photon, its 4-momentum is then  $k = (h\nu, 0, 0, h\nu)$ . After the interaction, the scattered photon has a 4-momentum

$$k' = \left( h\nu', \frac{h\nu'}{c} \sin\theta, 0, \frac{h\nu'}{c} \cos\theta \right)$$

while the one of the recoiling electron is then

$$p' = \left( E', -\frac{h\nu'}{c} \sin\theta, 0, -\frac{h\nu'}{c} \cos\theta \right)$$

assuming the scattering to happen in the x-z plane. Enforcing momentum conservation,

$$p + k = p' + k' \longrightarrow p + k - k' = p' \longrightarrow (p + k - k')^2 = (p')^2$$

and using the relativistic dispersion relations  $p^2 = m^2$  and  $k^2 = 0$ , the following chain of equalities is obtained:

$$\begin{aligned} (m^2 + 2pk - 2pk' - 2kk') &= m^2 \\ pk - pk' - kk' &= 0 \\ mc^2 \cdot h\nu - mc^2 \cdot h\nu' - h^2\nu\nu'(1 - \cos\theta) &= 0 \\ h\nu' &= \frac{h\nu}{1 - \frac{h\nu}{mc^2}(1 - \cos\theta)} \end{aligned}$$

It can be easily seen that the energy transfer is maximum when the photon is back-scattered ( $\theta = \pi$ ), while is minimum for  $\theta = 0^\circ$  and it's equal to zero. Simplifying the formula by introducing an adimensional variable  $\alpha = \frac{h\nu}{mc^2}$ , the expression for the energy of the scattered photon can be reexpressed as:

$$h\nu' = \frac{h\nu}{1 - \alpha \cdot (1 - \cos \theta)} \quad (1.2)$$

The energy of the recoiling electron is then

$$E_{e^-} = h\nu - h\nu' = h\nu \left( \frac{\alpha(1 - \cos \theta)}{1 + \alpha(1 - \cos \theta)} \right) \quad (1.3)$$

Now, taking the limit of Eq. 1.2 for  $\alpha \ll 1$  (which means  $E \ll mc^2$ , roughly 0.5 MeV),  $E' \approx E$ , which is the classical result.

Looking at the angles, two extreme cases must be analyzed. First, for  $\theta = 0$ ,  $h\nu' = h\nu'$  and so  $E_{e^-} = 0$ : indeed, the photon maintains its initial energy after the interaction and the transferred energy to the electron is almost zero. Instead, for  $\theta = \pi$ , there is the maximum energy transfer to the electron:

$$E_{e^-} = h\nu \left( \frac{2\alpha}{1 + 2\alpha} \right) \rightarrow E_{e^-} \approx \frac{mc^2}{2} \approx 0.25 \text{ MeV} \quad \text{for } \alpha \gg 1$$

## 1.2 Klein-Nishina formula

The probability of Compton interaction for a photon passing through a material is computable using the Compton scattering cross section. By definition, the differential cross section is the number of photons scattered in unit time and unit solid angle, divided by the incoming flux. The computation of the Compton cross section for scattering on a free electron was one of the first and most successfull result of quantum electrodynamics, and it was performed in 1928 by Klein and Nishina. The complete expression for the differential cross section is the following (for unpolarized photons):

$$\frac{d\sigma}{d\Omega} = \frac{r_0^2}{2} \cdot \frac{k'^2}{k} \left( \frac{k'}{k} + \frac{k}{k'} - \sin^2 \theta \right) \quad (1.4)$$

where  $k$  is the momentum of the incoming photon,  $k'$  is that of the outgoing one and  $r_0$  is the classical electron radius, defined in I.S as:

$$r_0 = \frac{e^2}{4\pi\epsilon_0} \cdot \frac{1}{m_e c^2}$$

In this case too, taking the low-energy limit of Eq. 1.4 (*i.e.* for  $k \ll m$ ,  $k \sim k'$ ), the classical differential Thomson cross section can be obtained:

$$\frac{d\sigma}{d\Omega} = \frac{r_0^2}{2} \cdot \frac{k'^2}{k} \left( \frac{k'}{k} + \frac{k}{k'} - \sin^2 \theta \right) \approx \frac{r_0^2}{2} \cdot (1 + \cos^2 \theta)$$

The formula can be extended to the case of the scattering on an electron bounded to an atom of atomic number  $Z$ . Making use of Eq. 1.2, computation gives the following result:

$$\frac{d\sigma}{d\Omega} = \frac{Z}{2} r_0^2 \left( \frac{1 + \cos^2 \theta}{1 + \alpha(1 - \cos \theta)} \right) \cdot \left( 1 + \frac{\alpha^2(1 - \cos \theta)^2}{(1 + \cos^2 \theta)[1 + \alpha(1 - \cos \theta)]} \right) \quad (1.5)$$

Fig. 1.2 shows how the Klein-Nishina's cross section changes with the energy of the incident photon. Looking at Fig. 1.2, it's evident that, for photons of low energy, scattering at  $0^\circ$  and  $180^\circ$  are equiprobable: Thomson scattering differential cross section indeed depends only on  $\cos^2 \theta$ . This isotropy breaks with increasing energy and forward direction is preferred.

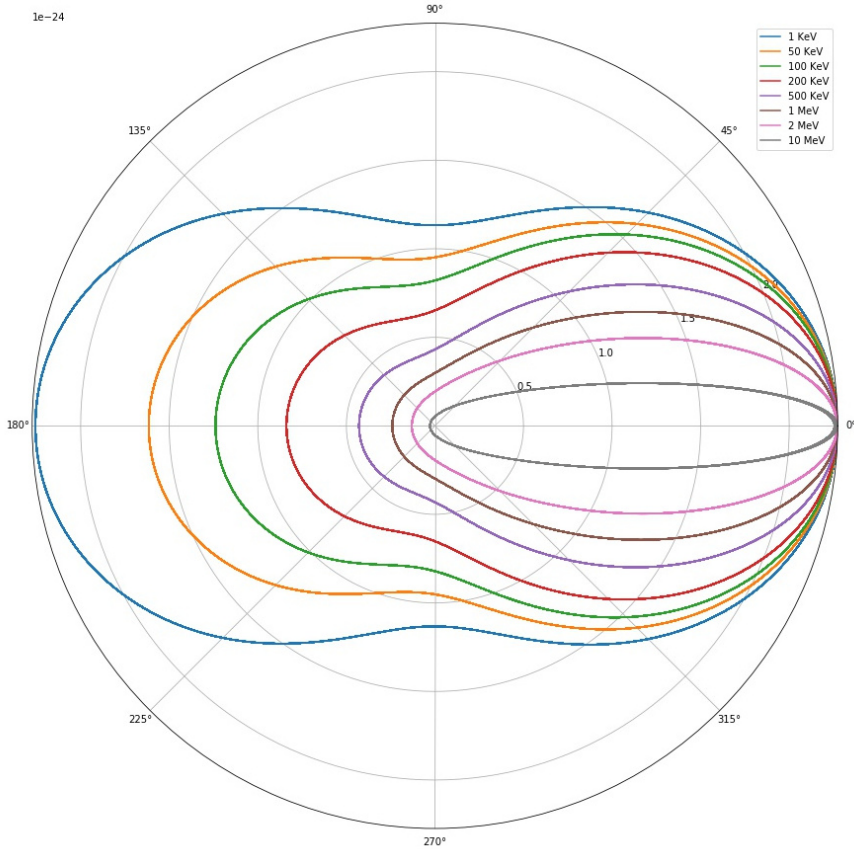


Figure 1.2: *Klein-Nishina's cross section in polar plot for incident  $\gamma$  at different energies.*

### 1.3 Positronium parity

Positron emitted in the  $^{22}\text{Na}$   $\beta^+$  decay loses almost all its kinetic energy in the crossed medium through coulombian interactions and *Bremsstrahlung* radiation, and then tends to form a bound state, called positronium, with one of the electrons of the medium.

A very interesting topic is the description of the decay phenomenology of the positronium, which depends on the relative polarization of the spins of the electron and the positron. Firstly, there are two possible spin states: the singlet state, denoted as  $^1S_0$ , called "para-positronium", and the triplet state,  $^3S_1$ , called "ortho-positronium". Since both these states are  $L = 0$  bound states of a fermion and its own antifermion, they are predicted by Dirac theory to be eigenstates of the parity operator  $P$  with eigenvalue  $-1$ . In fact:

$$P(e^+e^-) = (-1)^l \cdot P(e^+) \cdot P(e^-) = (-1)^{l+1} = -1$$

where it was used the fact that the parity of a fermion is opposite to the one of its own antifermion. Moreover, para-positronium ( $J = 0$ ), again according to Dirac theory, has positive C-parity: C-parity of a fermion-antifermion state is indeed  $(-1)^j$ . Therefore it must decay into an even number of photons, since C-parity of a system of  $n$  photons is  $(-1)^n$ . The most probable decay is obviously the one into two photons, each one of 511 keV. Lowest order Feynman graphs contributing to this decay are shown in Fig. 1.3.

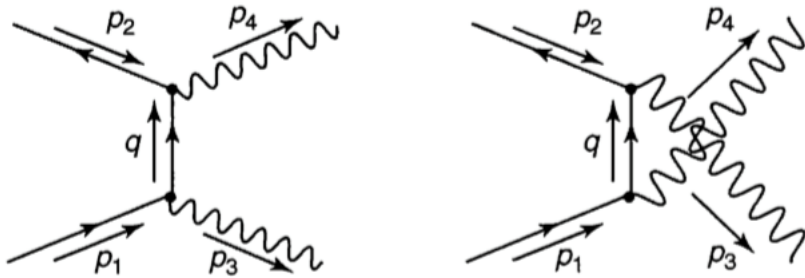


Figure 1.3: *Lowest order Feynman diagrams of para-positronium decay*

Lifetime of the singlet state is approximately:

$$\tau_0 = \frac{2\hbar}{m_e c^2 \alpha^5} \approx 0.1244 \text{ ns}$$

Ortho-positronium ( $J = 1$ ) has negative C-parity, so it decays in an odd number of photons, mostly three. Quantum Electrodynamics (QED) rules suppress this decay of a factor  $\alpha$  with respect to the one of the para-positronium, so lifetime of the triplet state is much longer and approximately equal to:

$$\tau_1 = \frac{4.5\hbar}{2m_e c^2 \alpha^6 (\pi^2 - 9)} \approx 138.6 \text{ ns}$$

The goal of this third part of the experiment is to verify the theoretical prediction of the parity of the positronium in the singlet state by analysing

the polarization of the emitted photons. Considering the triplet state, the proof of the theoretical prediction of the parity would be much more complicated because of the longer lifetime and of both theoretical and experimental difficulties in analysing a three-photons state.

The simplest forms for the wavefunctions of a two-photons state are given by the following equations:

$$\psi_1(2\gamma) = A(\vec{\epsilon}_1 \cdot \vec{\epsilon}_2) \propto \cos \alpha \quad (1.6)$$

$$\psi_2(2\gamma) = A(\vec{\epsilon}_1 \times \vec{\epsilon}_2) \propto \sin \alpha \quad (1.7)$$

where  $\alpha$  is the angle between the two polarization planes, *i.e.* the plane which contains the momentum of the photon  $\vec{k}$  and the polarization vector  $\vec{\epsilon}$ . Owing to the Bose-Einstein statistic of a set of identical bosons, both the wavefunctions must be totally symmetric under particle exchange, while spatial parities are opposite:  $\psi_1$  is odd and  $\psi_2$  is even, and they will be maximized by different values of  $\alpha$ , in particular  $\psi_1$  by  $\alpha = 0$  and  $\psi_2$  by  $\alpha = \pi/2$ . Expression of Compton differential cross section of Eq. 1.4 must be slightly modified to keep in account the polarization of the incoming photons, obtaining the following equation:

$$\frac{d\sigma}{d\Omega} = r_0^2 \left( \frac{h\nu'}{h\nu} \right)^2 \left( \frac{h\nu'}{h\nu} + \frac{h\nu}{h\nu'} - 2 \sin^2 \theta \cos^2 \phi \right) \quad (1.8)$$

where  $\phi$  is the angle between the scattering plane and the polarization vector  $\vec{\epsilon}$ .

$$\frac{d\sigma}{d\Omega} \Big|_{\phi=\pi/2} = \frac{5r_0^2}{16} \quad \text{and} \quad \frac{d\sigma}{d\Omega} \Big|_{\phi=0} = \frac{r_0^2}{16} \quad (1.9)$$

Looking at Eq. 1.9 it can be noted that Compton scattering at  $\theta = 90^\circ$ ,  $\phi = 90^\circ$  (photons orthogonally polarized), is five time more probable than the one at  $\theta = 90^\circ$ ,  $\phi = 0^\circ$  (photons longitudinally polarized). Compton interaction rate depends quite strongly on the polarization of the incoming photons and so on the initial parity of the positronium. In Sec. 3.4 it will be explained how to implement a measurement that depends on this physical quantity.

# Chapter 2

## Characterization

Before starting to perform Compton scattering measurements, it was necessary to check that the measurement system was working correctly by utilizing the same  $^{22}\text{Na}$  source.

In Fig. 2.1 a full spectrum of the  $^{22}\text{Na}$  source is shown. The interesting part of the spectrum is the one with energy around 511 keV and lower. It includes the full energy peak of the annihilation photons and the Compton and multi-Compton continuum zones.

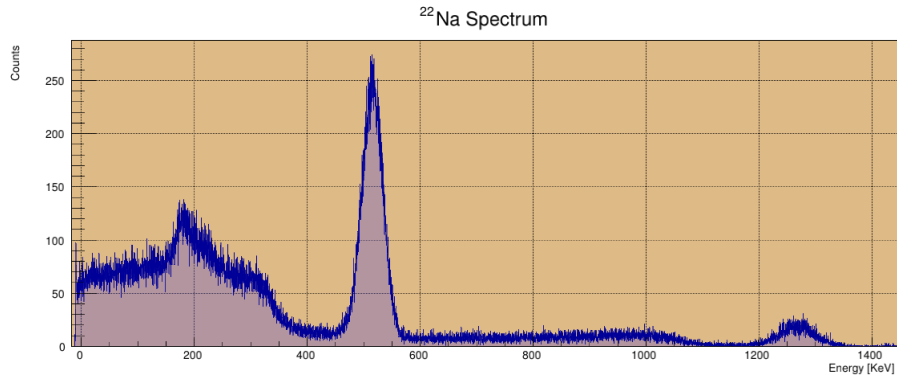


Figure 2.1: *Full  $^{22}\text{Na}$  spectrum. The highest peak is at 511 keV.*

The remaining portion of the spectrum is not important for the experiment purposes and will be cut at approximately 550 keV. Using a threshold around this value, the amplifier saturate for all the pulses associated to higher energy. In the characterization of the experimental setup, the focus was mainly on avoiding the generation of statistical noise and systematic errors in the measurements. All the main sources of error will be analyzed in the following sections, together with the optimization of the chain components, with the aim of obtaining a better resolution.

## 2.1 Experimental setup

Before starting with the characterization, all the components of the experimental setup are described. A complete scheme of the experimental setup, which includes source, detectors and all the electronic chain, is shown in Fig. 2.2. Each component will be fully described below.

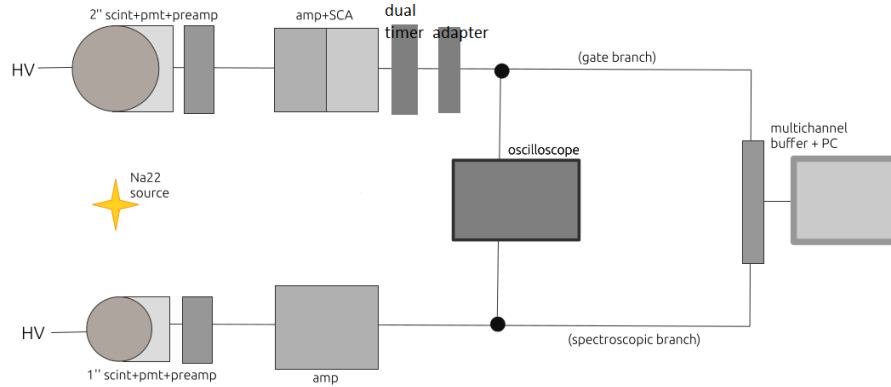


Figure 2.2: Complete scheme of the experimental setup.

Different types of devices were used in order to measure the energy of the photons and the interaction cross section. These devices are detailed in the following subsections.

### 2.1.1 Source



A radioactive source of  $^{22}\text{Na}$  is used for the production of photons.  $^{22}\text{Na}$  decays  $\beta^+$  *i.e* a proton in its nucleus decays into a neutron, a positron and an electron neutrino. The emitted positrons annihilate with electrons in the material causing the production of back-to-back photons in the gamma rays range of energy.

An important parameter used to characterize a source is the activity  $A$ , which is defined as the rate at which the isotope decays. The differential equation regulating the decay, that can be easily derived, is the following:

$$A = -\frac{dN}{dt} = \lambda \cdot N$$

where  $N$  is the number of nuclei and  $\lambda$  the decay constant. Its solution is:

$$N = N_0 e^{-\lambda t} \quad (2.1)$$

where  $N_0$  is the number of nuclei at time  $t = 0$ . The IS unit of the activity is the Bequerel (1 decay per second). Having an official certificate it was known that  $^{22}\text{Na}$  source employed in laboratory had an activity of 367.040 kBq ( $A_0$ )

measured on 26/09/2018. One is able to find out the current activity of the source using the fact that  $^{22}\text{Na}$ 's half-life is  $T_{1/2} = 2.6$  years. From Eq. 2.1:

$$\frac{N_0}{2} = N_0 e^{-\lambda T_{1/2}} \quad \longrightarrow \quad \lambda = \frac{\ln 2}{T_{1/2}}$$

So the current activity is:

$$A = A_0 2^{-t/T_{1/2}}$$

where  $t$  is the time's interval between the moment in which the measure is performed and 26/09/2018. Since the results in appendix A.5 are similar, an arithmetic average of all the values was used for all the measurements. This average resulted to be  $S_{av} = 190.68$  kBq. The standard deviation of the values was taken as uncertainty on the activity, and it was equal to  $\sigma_S = 3.83$  kBq. Fig. 2.3 shows a picture of  $^{22}\text{Na}$  source that was used during the experiment of Compton scattering.



Figure 2.3:  $^{22}\text{Na}$  source used in laboratory.

### 2.1.2 Detectors ~~A photon source~~

Two different scintillator detectors were used in order to observe the two back-to-back photons. A scintillator detects ionizing radiation thanks to the scintillation light produced in certain materials. The detectors were inorganic scintillators composed by sodium iodide, in which traces of thallium iodide (TII) were added. The absorption of energy results through the excitation of an electron from the valence band to the conduction band while the emission of photons by de-excitation of this electron can be observed through the passage from the conduction band to the valence band. Intrinsic NaI crystals have a high energy gap (5.8 eV), so emitted radiation is in the UV range, therefore it is not easily detectable. For this reason TII impurities, called activators, are added. By this way there will be energy states within the forbidden gap, through which electrons can de-excite back to the valence band. Since the difference in energy is significantly smaller than the original one, now the emitted photons are in the visible range.



Figure 2.4: 1" scintillator coupled with photomultiplier 905-1 Ortec (left) and 2" scintillator coupled with photomultiplier 905-3 Ortec (right).

Fig. 2.4 shows two NaI(Tl) detectors of different size that were used in laboratory. The thinnest one has a diameter of 2.54 cm (1") and is 2.54 cm thick while the thickest has a diameter of 5.08 cm (2") and is 5.08 cm thick. Some lead bricks were used to shield the scintillators from environmental radiation.

### 2.1.3 Photomultipliers and Preamplifier

**Photomultipliers** In the experiment, two photomultiplier tubes coupled with the two scintillators were used. In particular a  $\gamma$ -photon interaction with a scintillator detector produces a pulse of light that is converted into an electric pulse by the photomultiplier tube (PMT), that operates thanks to the photoelectric effect. This device is a tube, made usually by glass, composed by an enter window, where light enters, a photocathode, from which photons can extract the electrons, a system of electrodes, which allows the acceleration of electrons and their focalization on the first dynode, and then 10 dynodes that multiply the number of electrons striking on each of them. By this way an electronic multiplication occurs, that leads to a gain between  $10^3$  and  $10^8$ . The process ends with the collection of all the electrons by an anodic grid. PMTs are fast and linear devices with huge gain and low noise. The electrode tensions are generated by a high tension supplier connected to a resistive tension divider.

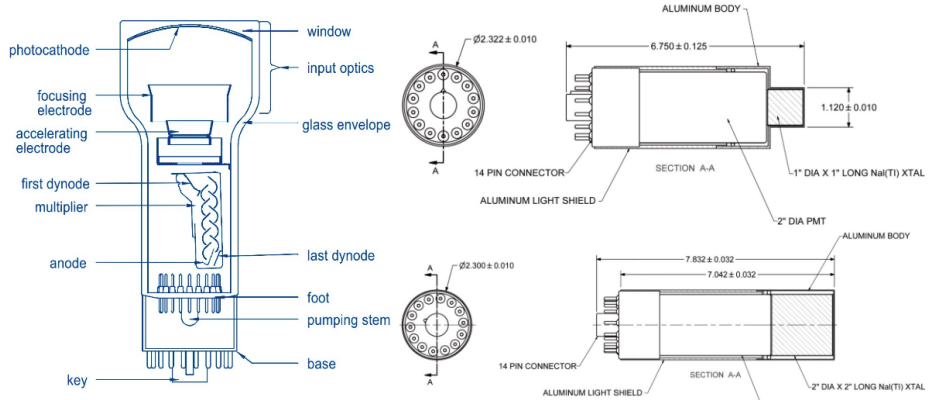


Figure 2.5: *Working scheme of: a photomultiplier (left), a PMT coupled with 1" scintillator (on the top right) and a PMT coupled with 2" scintillator (on the bottom right).*

Fig. 2.5 shows a working scheme of PMT and the dimensions of PMTs used in the experiment. Since the photocathodes of both the PMTs have a 2" diameter, the thinnest scintillator (1" diameter) uses only the central zone of the photocathode.

**Preamplifier** A preamplifier is the first component in a signal processing chain of a radiation detector. It is placed next to the scintillator and acts as an interface between the detector and the pulse processing electronics that follow. The main function of a preamplifier is to optimize the time constants of the pulses. It shapes the pulse keeping a short rise time, which corresponds to the charge collection time, and setting a long decay time, fixed by its own time constant,  $\tau = RC$ .

The two preamplifiers, one for each scintillator, that were used were ORTEC Model 276. A picture of a such a type of preamplifier is shown in Fig. 2.6. It has a diameter of 5.58 cm and it is 10.1 cm long. The model 276 has a diode protection network to prevent damage to the internal transistors due to sudden application or removal of high voltage to the unit.



Figure 2.6: *The ORTEC Model 276 Photomultiplier Tube Base and Preamplifier.*

### 2.1.4 Electronic Chain

A part of the electronic chain that was used during the experiment is shown in Fig. 2.7.



Figure 2.7: *Electronic chain setup from amplifier to oscilloscope (left out) used in laboratory.*



Figure 2.8: *ORTEC Model 570 Amplifier.*

**Amplifier** The amplifier is responsible for the main amplification of the signal. In this experiment the ORTEC amplifier model 570, shown in Fig. 2.8, was used. It is characterized by low noise ( $< 5 \mu V$ ) and wide-gain range, adjustable from 1 to 1500. The model 570 incorporates an automatic threshold control and an automatic gated baseline restorer, which allows the system resolution to be nearly independent of the input counting rate. The output of the amplifier, thanks to active filter networks, is unipolar with optimal signal-to-noise ratio over a wide range of time constants. In addition, the DC stability of the model 570 output eliminates the spectrum broadening caused by the DC drift.

**Power supply** A power supply is an electrical device that converts electric current from a source to the correct voltage, current, and frequency to power the load. In the setup the CAEN Model N1470A was used, which is shown in Fig. 2.9. The Model N1470A has 2 independent high voltage channels. Each channel provides a  $\pm 8$  kV maximum voltage, a 3 mA maximum current and a 9 W maximum power. There is the overcurrent detection: if a channel tries to draw a current larger than its programmed limit, it enters the TRIP status, keeping the maximum allowed value for a programmable time (TRIP), before being switched off.

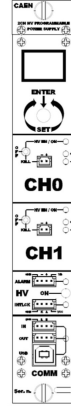


Figure 2.9: *CAEN Model N1470A Power Supply*.



Figure 2.10: *ORTEC Model 551 TiSCA*.

**TiSCA** TiSCA means Timing Single Channel Analyzer. It generates an impulse whenever the scintillators, in coincidence mode, detect a signal in the correct range of energies. The ORTEC TiSCA model 551 performs the dual functions of single-channel pulse-height analysis and timing signal derivation. A picture of this model is shown in Fig. 2.10. In particular a logic signal is generated whenever the amplified unipolar signal falls within the energy window set by the front-panel controls ( $E$  and  $\Delta E$ ). The TiSCA also uses leading-edge timing to provide the output logic signal in time correlation with the input one. The user can set the energy range, in which the logical signal is generated, through two controls: the Lower Level ( $E$ ), adjustable from 0 to 10 V, that determines the threshold setting for the lower-level discriminator and the Window ( $\Delta E$ ), adjustable from 0 to 1 V, that regulates the width of the acceptance range. In this experiment the energy window was chosen in order to include the peak of 511 keV photons.

**Adapter and Dual Timer** The adapter is divided into four sections: the two upper sections, which were used in laboratory, perform the NIM-to-TTL conversion (8 channels) while the two lower sections perform the TTL-to-NIM conversion (8 channels). In each section a two-position switch allows logic conversion. The CAEN Model N89 adapter was used in laboratory.

The dual timer consists of two identical triggered pulse generator. They produce fast NIM and ECL pulses with adjustable width from 50 ns to 10 s, and retriggerable before the end of the output signal. The CAEN Model 93B dual timer was used in laboratory. Both the adapter and the dual timer are shown in Fig. 2.11.



Figure 2.11: *CAEN Model 93B Dual Timer (left) and CAEN Model N89 Adapter (right).*

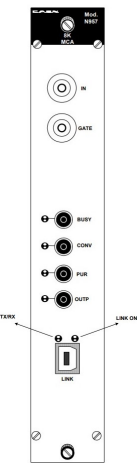


Figure 2.12:  
*CAEN Model N957 MCA.*

**MCA** MCA stands for Multiple-Channel Analyzer. It is used to perform a spectroscopic analysis of the incoming signals. For Compton scattering spectroscopy MCA was used in Pulse-Height Analysis (PCA) mode. It counts the pulses and sorts them into a 8192-bins (channels) histogram (or spectrum) of number of events in unit pulse height ( $\frac{dN}{dH}$ ), versus pulse-height, measured in Volts. The spectrum was acquired using the Gate mode to allow the selection of signals whose peaks occur at least  $0.2 \mu\text{s}$  before the end and after the beginning of the logical step. In the input stage of the module, there is a detection of the input peak value, while the gate is active, and it is kept in standby until the ADC ends the conversion. Conversion can be triggered automatically (Auto Gate mode) or externally (External Gated Mode). In the first case a discriminator, with a threshold, enables the conversion, which is active as long as the amplitude of the input signal is above such threshold. In the latter, the external gate is fed to the module. The Fig. 2.12 shows the CAEN Model N957 MCA that was used in laboratory.

## 2.2 MCA linearity

The Multichannel-Analyzer (MCA) is the component of the electronic chain which is used to perform a spectroscopic analysis of the incoming signals. It divides the different codes into their respective  $2^n$  channels. In this case the MCA also includes the ADC, which transforms the signals coming from the amplifier into shorter or longer bit sequences according to the number of channels chosen to divide the spectrum.

The choice of the spectrum binning depends on two factors: the discrete spectrum should reproduce at best the ideal continuum spectrum, so a larger number of channels is preferable to better resolve the spectrum structures (as a general rule, at least 4-5 channels corresponding to the FWHM of the peak are required). On the other side, an excessive one leads to a low amount of counts in each channel, increasing the statistical fluctuations and worsening the resolution. For this experiment, since the MCA has up to 8192 bins available, an intermediate choice was done, namely 1024 channels, to optimize the statistics too.

The digital conversion of the ADC has to be linear, with one channel corresponding to each voltage, otherwise a different conversion gain for various voltages would result in a spectrum deformation.

Generally, there is a greater deviation from linearity at low and high voltages; for this reason, considering the former, an offset is always added not to start from the full-scale and, for the latter, the values of the last channels in the saturation zone are not kept in account in the measurements. Typically, the MCA input voltage ranges from 0 to 10 V and so a pulse generator with different amplitudes lying in this range was used to verify its linearity. The graph in Fig. 2.13 shows the linearity trend of the MCA for different amplitudes.

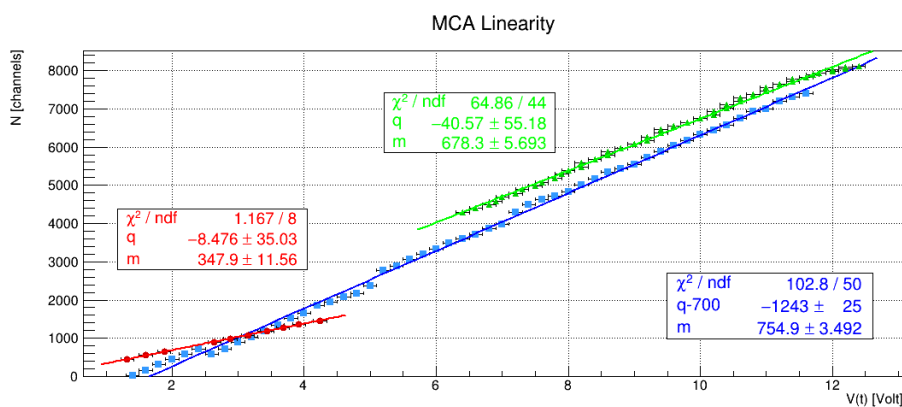


Figure 2.13: Linearity of the MCA for different voltage values (on the x axis) and different frequency values (red, blue and green).

The fit returns the line's slope which corresponds to the conversion gain (voltage-channel) and the intercept which corresponds to the offset linked to the first channel (minimum voltage that corresponds to channel 0). The green and red fit in Fig. 2.13 are measurements taken separately because, in addition to varying the voltage, the frequency of the test pulse was also varied and this led to different slopes.

Anyway, whatever is the gain or the offset, it can be seen that the MCA was linear with a small fluctuation and only in the last channels there was a deviation from linearity by some percentage value.

## 2.3 Resolution

The detector does not measure with infinite precision, but there are several factors contributing to the total uncertainty. They can be divided into two categories: statistical and systematical errors. The most important source of statistical uncertainty is the intrinsically stochastic nature of the photoelectrons production at the photocathode. Indeed, this process follows an approximately poissonian Law, so that, for a given amount of delivered energy  $E$ , the mean number of charge carriers produced is:

$$N = \frac{E}{W} \quad (2.2)$$

where  $W$  is the mean energy necessary to extract an electron from the material. Being a poissonian process, the variance of  $N$  is then:

$$\sigma_N = \sqrt{N}$$

And so, from Eq. 2.2

$$\frac{\sigma_E}{E} = \frac{\sigma_N}{N} = \frac{1}{\sqrt{N}}$$

The energy resolution of the system can be defined as:

$$R_E \equiv \frac{(FWHM)_E}{E} = 2.35 \frac{\sigma_E}{E} = \frac{2.35}{\sqrt{N}} \propto \frac{1}{\sqrt{E}}$$

where FWHM is the full width at half maximum of the energy peak. Note that the gaussian approximation of the Poisson distribution was used. Therefore energy resolution is expected to decrease with energy and so with the voltage supply of the PMT. Other reasons of the deterioration of the resolution can be spurious noise pulses, gain instability of the PMT or of the electronic chain, photocathode imperfections and many others. The main sources of noise pulses are environmental radioactivity and thermoionic emission. For the former, active and passive shielding methods were adopted, as mentioned in Sec. 2.1. For what concerns the latter, the intensity of the so

called “dark current” (current flowing to the anode with the cathode off) of thermically extracted electrons obviously increases with the temperature, so it depends on the voltage supply too (Joule effect).

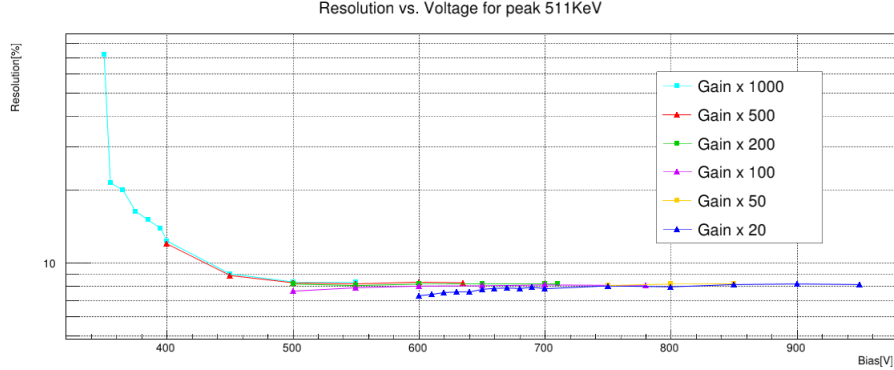


Figure 2.14: *Different resolution curves of 1" detector for different amplifier gains in logarithmic scale.*

Voltage[V]	Resolution	$\delta_R$
600	7.32E-02	3.76E-04
610	7.41E-02	3.73E-04
620	7.54E-02	4.32E-04
630	7.59E-02	3.62E-04
640	7.58E-02	3.73E-04
650	7.78E-02	3.74E-04
660	7.85E-02	4.85E-04
670	7.88E-02	3.98E-04
680	7.84E-02	4.47E-04
690	7.93E-02	4.38E-04
700	7.82E-02	4.46E-04
750	8.04E-02	4.79E-04
800	7.97E-02	3.24E-04
850	8.14E-02	3.11E-04
900	8.18E-02	4.19E-04
950	8.14E-02	3.04E-04

Table 2.1: *Resolution with own error for different PMT voltages.*

The importance of the photomultiplier (PMT) power supply voltage depends also on the fact that, when the electrons leave the photocathode, they must have sufficient energy to extract secondary electrons from the first dynode, giving life to an electron avalanche. In average, the gain at each dynode, is roughly equal to 5 photoelectrons produced for each incident one. The total amount of free charge should be large enough to produce a measurable signal on the anode, but it should still maintain a certain proportionality with the energy deposited by the particle in the scintillator. Low voltages do not allow the cascade production of electrons (low probability of escaping the surface potential barrier of the material) while, on contrary, high voltages lead the electrons to penetrate the dynodes for a depth greater than the mean free path of the electron in the material (so it has low probability of exiting the dynode), lowering the efficiency of the process.

Consequently, there is a useful voltage range where the photomultiplier can work.

Generally the voltage difference between each dynode is about 100 V, but this value can variate depending on the number of multiplication steps. Therefore in Fig. 2.14 there is a plot that shows the variation of the resolution for different gain values of the amplifier as a function of the voltage supply.

From Fig. 2.14, it can be seen that the gain of the amplifier does not substantially vary the value of the resolution, which depends just on the voltage. Beyond 500 V there is no resolution improvement up to about 1000 V, as shown in Tab. 2.1.

For each gain value of the amplifier, there is a cut-off in voltage, above which resolution cannot be evaluated, because the 511 keV signal makes the amplifier saturate, as mentioned in Sec. 2. 830 V was chosen as the supply voltage of the PMT for a fixed gain ( $G = 25$ ).

## 2.4 Shaping time

In each amplifier it is possible to fix the pulse shaping time, *i.e.* the time width of the signal. The choice of the shaping time depends on the optimization of three main parameters:

- The ballistic deficit, *i.e.* a systematic error that occurs in the evaluation of the signal amplitude that is recorded constantly lower than the true one. This happens if the amplifier restores the baseline before the actual peak of the signal is reached.
- The pile-up, which is the time overlap of two or more consecutive pulses, that may not be resolved by the ADC.
- The signal-to-noise ratio, which is defined as the ratio of the power output of the signal over the one of the noise.

Therefore, the choice of the signal shaping time is a fundamental step for the correct analysis of the spectrum in order to have a signal readable by the ADC. In addition to set a fixed voltage gain to the signal, the linear amplifier can modify the shape of the rise and fall of the signal.

The presence of capacitance, inductances and parasitic resistances attenuates some frequencies with respect to others with a consequent modification of the spectrum. To overcome this problem, each module in the chain has the following features: an high input impedance to avoid disturbing the signal and a low output impedance to minimize signal losses. The frequency spectrum of the noise is extremely broad and can be considered uniformly distributed (white noise) while the signal covers a narrow frequency band.

VEDERE  
TOGLI

The shaping time choice aims to remove the problem of statistical fluctuations of the baseline, due to low-frequency noise, that can lead to a biased evaluation of the amplitude of the signal. However, the pulse coming from the preamplifier is already partially shaped: indeed, in this experiment, the main task of the preamplifier is not the amplification of the signal collected by the PMT (which is already a high one) but, above all, to fix the  $RC$  constant (the decay time of the pulses). In this way, the signals have tails up to  $50 \mu s$ , which are sufficiently long to avoid ballistic deficit. The task of the linear amplifier is therefore to shape the signal by reducing the decay time once the peak amplitude is exceeded to avoid pile-up.

There are several possible shapes of the signal but the gaussian one was the most suitable for this experiment: it is symmetrical, it maximizes the signal-to-noise ratio, it does not peak at a single point and it returns quite quickly to the baseline. To check which is the best width of this signal, it is plotted in function of the resolution or, more precisely, of the FWHM, as showed in Fig. 2.15.

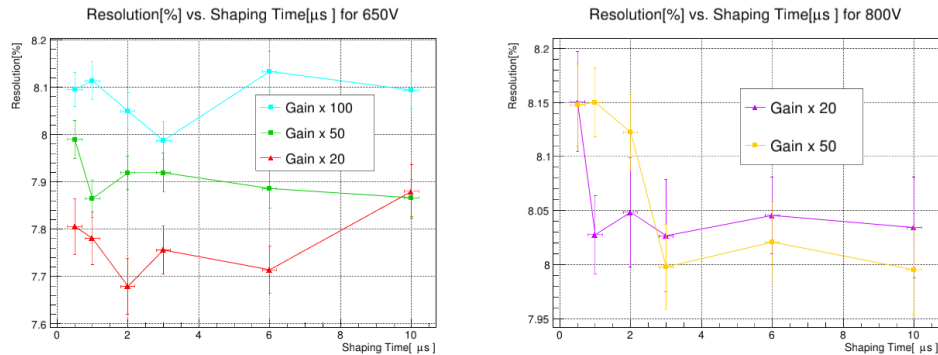


Figure 2.15: On the left, the trend of the energy resolution as a function of the signal shaping time for three different gains at fixed voltage (650 V). On the right the same trend for another fixed voltage (800 V).

The Gaussian shaping is defined as:

$$(CR - (RC)^N)$$

where  $CR$  and  $RC$  are differential and integrator impedance dividers. The Gaussian shaping peaks at  $t = N \cdot \tau$ , where  $\tau$  is the time constant of the  $RC$  filter. The amplifier gives the possibility to choose different shaping times: from  $0.5 \mu s$  up to  $10 \mu s$ . As previously explained, short shaping time would lead to a ballistic deficit with consequent increase of the uncertainty on the value of  $V_{max}$  (the peak amplitude of the pulse) and a worse resolution, as it can be seen in Fig. 2.15. Furthermore, the presence of electronic components leads to higher voltage fluctuations (noise in series) at short shaping time.

Perché abbiamo variato il voltaggio e il gain?  
 Non ho capito cosa succede se il gain/voltaggio  
 sono troppo alti o troppo bassi, il voltaggio  
 parso sia la cosa del capitolo prima.

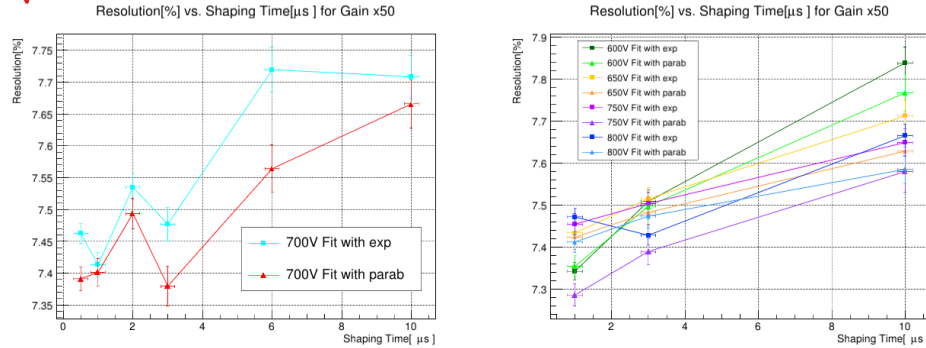


Figure 2.16: On the left, the trend of the energy resolution as a function of the signal shaping for two different types of fit at fixed voltage and gain. On the right the same trend according to the type of fit for different power supply voltage values for a fixed gain.

On the other hand, a long shaping time determinates a worsening of the resolution due to an increase of both pile-up events and dead time, with a concurrent raise of the loss of counts. Furthermore, longer shaping times lead to a worse signal-to-noise ratio with an increase in parallel noise and leakage current. Therefore, there are optimal values for both high and low counting rates that can be experimentally determined.

Voltage[V] = 650V				Voltage[V] = 800V				
Gain x20		Gain x50		Gain x20		Gain x50		
Shaping [μs]	R [%]	$\sigma_R$	R [%]	$\sigma_R$	R [%]	$\sigma_R$	R [%]	$\sigma_R$
0.5	7.81	5.91e-02	7.99	4.01e-02	8.15	4.63e-02	8.15	3.80e-02
1	7.68	5.91e-02	7.92	3.51e-02	8.05	5.06e-02	8.12	3.53e-02
2	7.76	5.04e-02	7.92	4.12e-02	8.03	5.21e-02	8.00	3.97e-02
3	7.71	5.06e-02	7.89	4.21e-02	8.05	3.55e-02	8.02	3.70e-02
6	7.88	5.62e-02	7.87	3.94e-02	8.03	4.67e-02	8.00	4.11e-02
10	7.78	5.54e-02	7.86	3.93e-02	8.03	3.62e-02	8.15	3.19e-02

Table 2.2: Resolution for different voltages of the PMT as a function of the signal shaping with relative error.

Since the measuring apparatus works in coincidence with a scintillator used as a linear gate coupled with a TiSCA, which allows to select only the signals that fall within the useful energy range (around 511 keV), it was observed, from the oscilloscope, that at high shaping time the rise time was too long. What should happen is that the signal falls within the limits of the square wave coming from the TiSCA.

There is no interest in the information contained in the rise of the signal and, moreover, long shaping time would have brought the  $V_{max}$  to several  $\mu s$  of delay and this would have required an elongation of the gate pulse (the square wave). In order not to keep the gate open for too long and not to have the peak after the gate had closed, a  $1 \mu s$  shaping time was chosen. The different graphs in Fig. 2.15 and Fig. 2.16 show that there is not the expected strong dependence of resolution on the shaping time: the expected optimal value is not evident, as it can be seen looking at the results in Tab. 2.2. However, the reduced activity of the source combined with both the small solid angle spanned by the detector and the energy selection of the pulses led to a counting rate low enough not to compromise the resolution even for a long shaping time.

## 2.5 Coincidence and autocoincidence

The back-to-back emission of annihilation photons from positronium was exploited to set the system in time and energy coincidence. The goal of this active shielding technique is to reduce the background (especially the Compton continuum) produced by the environmental radiation which would be required to be completely separated from the signal of interest. The coincidence technique consists in splitting the acquisition chain in two branches: a logical gate opening signal travels in the first, while the signal for spectroscopy, that will enter the MCA, in the second. This is based on the fact that, when a signal arrives, the gate opens for a certain amount of time and, as long as the gate is open, any signal that reaches the 1" detector can be recorded. Moreover, in order to open the gate, a signal whose energy lies in a fixed interval around 511 keV is needed, so that all the other background signals, of different energy, are not detected. Therefore incoming signals undergo a timing selection, *i.e.* the signal is recorded only if it temporally coincides with the gate one, but also energy one, *i.e.* only a 511 keV signal can open the gate.

Looking at the electronics, since the ADC has a dead time to record the signal, given two coinciding events, it is necessary that the one on the gate branch anticipates of about  $0.5 \mu s$  the other on the spectroscopy branch. Consequently, the signal on the latter branch was delayed through a suitable choice of the shaping time. Basing on it, it was decided how much to lengthen the square wave that would have kept the gate open. It was therefore decided to take a value of about  $2 \mu s$ , as shown in Fig. 2.17.

It should be noted that precision in time coincidence is certainly more significant than achieving maximum resolution because it is desired that only one signal can enter during this time interval, otherwise, the sense of coincidences would be lost. Anyway pile-up problems were solved thanks to the low activity of the source and to the small solid angle of the gate

scintillator and therefore they were not considered.

To verify that the MCA acquires correctly, it was necessary to make a comparison with the MAESTRO software in acquisition mode with active gate (coincidence). The procedure was performed using only the gate scintillator, so that the temporal coincidence is definitely verified (self-coincidence).

After connecting the 2" detector to the counting branch, it was necessary to decide the amplitude window of the TISCA, considering the gain of the amplifier.

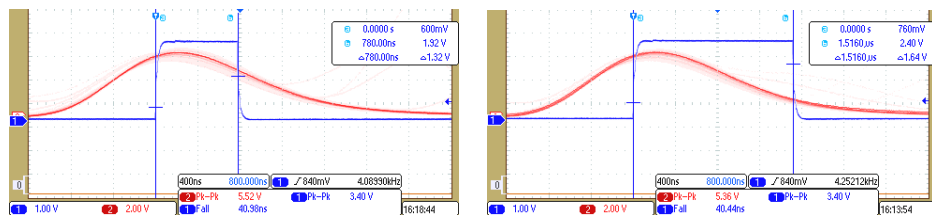


Figure 2.17: *Overlap seen by the oscilloscope of the two signals. In red the signal formed and in blue the square wave. Once the shape of the signal has been fixed, TISCA adjusts the time interval for the opening of the gate, i.e., the width of the square wave.*

The photon that interacts with the gate produces a signal which, if collected at the PMT anode, is not completely shaped by the preamplifier. This signal, then, takes the shape of a typical fast signal due to the collection of electrons. In order to avoid reflection along the coaxial cables that have a standard resistance of  $50 \Omega$ , a  $50 \Omega$  plug was placed in parallel with the anode output impedance in order to reduce the impedance difference and get a readable signal.

Then, the signal arrives at the TiSCA which, in this case, can provide a gain to the signal. At the output, a square wave signal of constant amplitude was obtained, equal for each signal, whose duration was chosen to be greater than the rise time of the signal, in order to allow the recording of the maximum amplitude of the signal on the other branch (as explained in the Sec. 2.5).

This gate aimed to keep the ADC of the MCA open for the entire duration of the pulse in order to record only the signals that occur during the timerange of the square wave. The goal of such a coincidence system is clearly the reduction of background spurious signals.

However, in order to select the significant pulses among all arriving at the gate, i.e. those with an energy around 511 keV, and to prevent the gate from opening for each background event (Compton scattering, environmental radiation or the characteristic  $\gamma$  of  $^{22}\text{Na}$ ), all these signals must be discarded by the TISCA. So, at the preamplifier output of the two-inch detector, a T-connection splits the signal (the signal will be half of the initial one on

each of the branches): the former of the obtained pulses is amplified and enters the MCA, contributing to the energy spectrum, while the latter enters the TiSCA and it is used, as said before, as a gate pulse. Varying the width of TiSCA window (window width, lower level) the MCA spectrum can be “cleaned” by cancelling all the signals that do not fall within about  $3\sigma$  from the peak identified as the 511 keV one ( $\sigma$  was evaluated with the gaussian fit of the peak). By this way, the gate will only open for signals in a narrow energy range.

Once the windows had been arranged, it was necessary to return from the autocoincidence configuration, in which the detector acts both as a gate and a spectrometer, to the initial configuration with two detectors. In this step it must be considered that, in order to choose the correct energy range, the signal had been splitted in two parts and, therefore, at the input of the amplifier branch there was a characteristic impedance that moved the peak from 511 keV out of the interval selected by the TISCA in coincidence mode. To solve this problem, a resistance connected to ground of  $1000 \Omega$  was inserted to simulate the connection to the amplifier. The graph in Fig. 2.18 shows the position of the peak with and without the characteristic impedance.

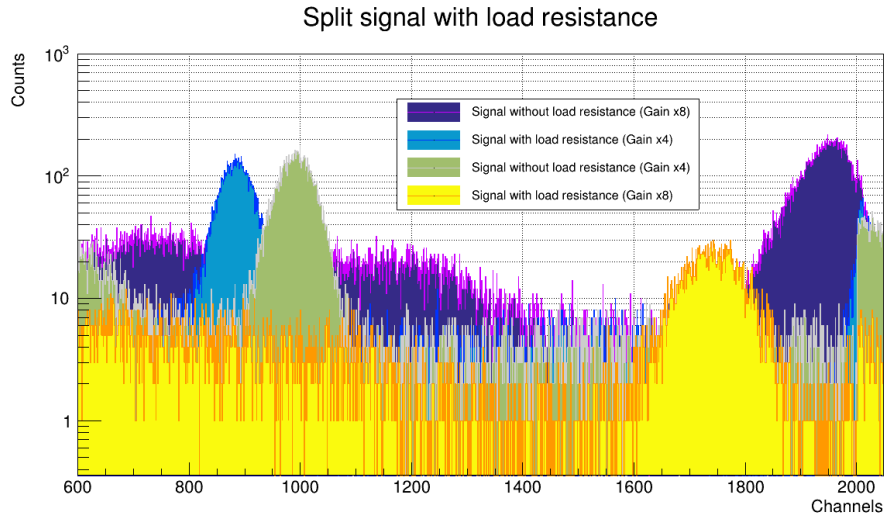


Figure 2.18: 511 keV peak and sodium  $\gamma$  peak shift in presence or absence of load resistance for two different gain values. Width and distance between peaks depend on the gain of the amplifier.

As it can be clearly seen, the peak position is shifted of about one hundred channels over a 2048 channel binning for low gain values, and the difference increases with increasing gain. It was also verified that the width of the square wave of the gate, even if lengthened or shortened (keeping  $V_{max}$  inside), did not change the number of counts in the MCA peak.

This window selection procedure was repeated several times because of the sensitivity of the cursor movement and the lack of possibility to obtain a symmetrical window around the peak. Furthermore, in the cut area, which therefore should have ideally zero counts, channels were still filled. At the end it was decided to replace the module that acted as both amplifier and TiSCA with a series of modules. However, the defective module was used as an amplifier while the TiSCA output was replaced by a dual-timer. This last device aimed to lengthen or shorten the square associated with the SCA. The dual-timer in turn is associated with the adapter, that converts the NIM standard to TTL because the MCA requires a positive polarity.

## 2.6 Energy calibration

The electric signal, which is produced by the scintillator and the photomultiplier, is converted by the ADC in a binary code stored in one channel of the MCA. The number of the channel is proportional to the signal amplitude and, therefore, to the charge produced by the radiation. Since the charge is proportional to the radiation energy, the channel number is a linear function of the delivered energy.

A calibration is necessary in order to convert ADC spectrum into an energy spectrum. In the experiment, different calibration sources with different  $\gamma$  peaks were used. Hence, knowing energy values of the peaks for each type of source and plotting them against their position in the ADC spectrum, a linear relationship can be extrapolated. The features of different detected peaks are shown in Tab. 2.3.

Elements	Channels	Expected Energy[KeV]	$\delta_{ch}$
$^{57}Co$	60.7102	14.413	0.20372
$^{241}Am$	75.8486	26.345	0.32880
$^{237}Np$	122.966	29.374	0.59635
$^{241}Am$	234.391	59.541	0.14496
$^{44}Ti$	257.750	67.875	0.07935
$^{228}Th$	289.925	84.373	0.42863
$^{44}Ti$	298.968	78.337	0.05814
$^{57}Co$	441.213	122.061	0.06845
$^{212}Pb$	821.391	239.000	0.27887
$^{22}Na$	1674.25	510.998	0.12593
$^{208}Tl$	1919.72	583.200	1.70441

Table 2.3: Values of  $\gamma$  peaks in ADC (channels) and energy (keV) for different materials.

The amplifier gain was set in order to place the energy region of interest in the MCA's range of linearity. As it can be seen in Fig. 2.19, the gain was chosen to place the 511 keV peak of  $^{22}\text{Na}$  around the channel 1700. By this way, it is far enough along the spectrum to fit the others less energetic peaks. In Fig. 2.19 an example of a non-calibrated spectrum for  $^{241}\text{Am}$  is shown.

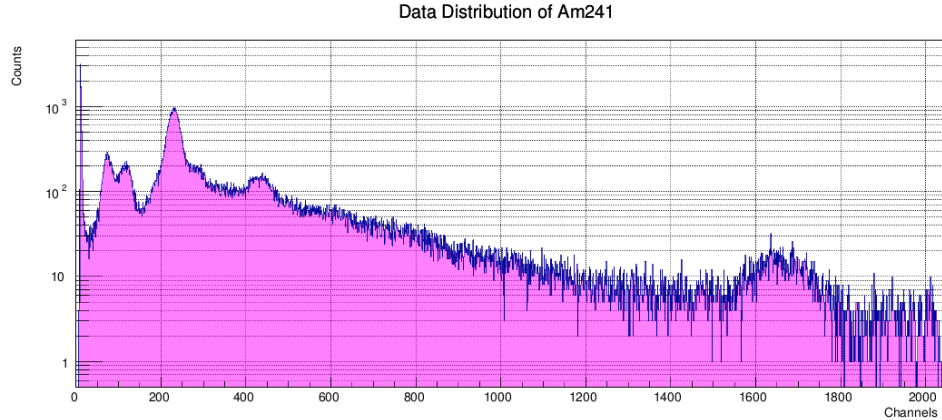


Figure 2.19: Plot of non-calibrated ADC spectrum for  $^{241}\text{Am}$ .

The first step of the calibration is a gaussian fit of peaks with different energies in the ADC spectrum for each source. It can be noticed that due to the spectrum background, caused by both electronic chain and dark current, an exponential function (or a polynomial function) was added to the previous gaussian one. The fit function is:

$$f(x) = p[0] + p[1]e^{-\frac{1}{2} \frac{(x-p[2])^2}{p[3]^2}} + e^{p[4]+p[5]x} \quad (\text{or, } p[4]x^2 + p[5]x + p[6])$$

where  $p[0], p[1], p[2], p[3], p[4], p[5], p[6]$  are fit parameters. An example of this fit is shown in Fig. 2.20.

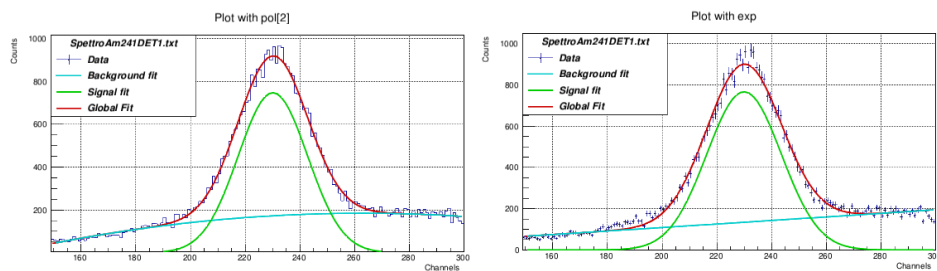


Figure 2.20: Plot of ADC spectrum for  $^{241}\text{Am}$  with a zoom on a peak fitted with gaussian plus exponential function (right) or gaussian plus polynomial function (left).

At this point, fit parameters were extrapolated and, in particular, the gaussian mean for every peak, which gave the position of the peak in ADC spectrum. The peaks values in energy (keV) were plotted against the peaks position in ADC and, at the end, a linear fit was made. For the 1" scintillator, an example of this fit with different sources is shown in Fig. 2.21. Then, the angular coefficient and the y-axis intercept with their errors were extrapolated from the linear fit.

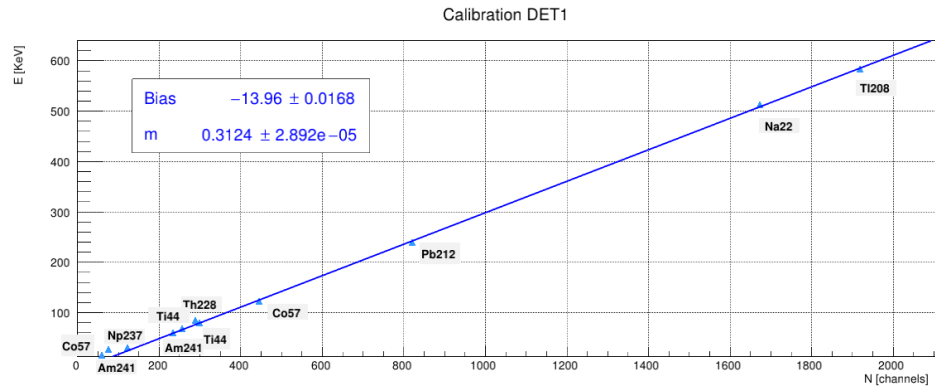


Figure 2.21: *Calibration line of the thin detector. Each point corresponds to one peak referred to a specific source.*

The linear fit formula is:

$$p(\text{keV}) = m \cdot p(\text{ADC}) + q \quad (2.3)$$

where:  $m$  is the angular coefficient,  $q$  is the intercept with y axis,  $P(\text{ADC})$  and  $P(\text{keV})$  are ADC and energy peaks.

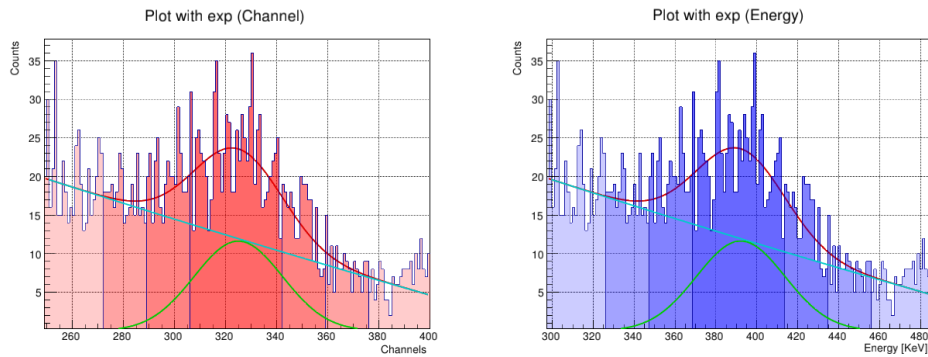


Figure 2.22: *Plot of a non-calibrated ADC spectrum (left) and a calibrated energy spectrum (right).*

By applying the Eq. 2.3 to ADC spectrum for each source the energy spectrum was finally obtained. In Fig. 2.22 an example of a calibrated energy spectrum is shown. The final fit parameters that were used to calibrate spectrum of the thin detector are shown in Tab. 2.4.

Detector	m	$\delta_m$	q	$\delta_q$
thin	0.312	2.892e-05	-13.96	0.017

Table 2.4: Value of angular coefficient ( $m$ ) and intercept with  $y$  axis ( $q$ ) with their errors.

## 2.7 Efficiency

One of the most critical points of detectors characterization is the evaluation of their efficiency. The detection efficiency is a measure of the percentage of the overall radiation emitted by a source, that a given detector manages to detect. The measure of the efficiency of the detection system is fundamental to compute the differential cross section of the scattering and verify then the Klein-Nishina formula.

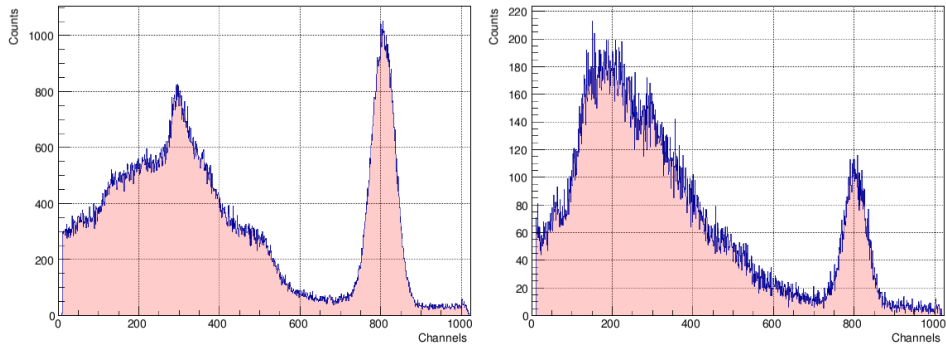


Figure 2.23: Spectra at two different distances of the thinnest detector: 15 cm (left) and 50 cm (right).

Indeed, as reported in Sec. 3.3, the product of the efficiencies of the two detectors appears among the parameters of Eq. 3.5, that relates the detected rate to the differential cross section. The evaluation of each of the two parameters was performed in the simplest possible configuration: both the scintillators were set in autogate mode and the source was placed between them, so that each of the two can collect spectra independently. In this setup, the rate measured by the  $i^{th}$  spectrometer is:

$$n = \epsilon_i \cdot 2S \cdot BR \cdot \frac{\Delta\Omega_1}{4\pi} \quad (2.4)$$

where  $\epsilon_i$  is the intrinsic efficiency of the respective detector,  $S$  is the activity of the source and  $BR$  is the branching ratio of the  $^{22}\text{Na}$   $\beta^+$  decay and  $\Delta\Omega_1$  is the solid angle subtended by the spectrometer.

The determination of  $\epsilon_i$  was performed just by changing the distance between the source and each of the scintillators (and so the subtended solid angle too) and measuring the detected rate at the various distances. The distances used for the measurements were 15, 20, 25, 30, 35 and 50 cm. In Fig. 2.23 an example of two spectra at two different distances is shown, hence 15 and 50 cm.

It can be noticed that at smaller distances counts are fewer than at larger ones, as obviously expected from the difference in the subtended solid angle. With a linear fit of the plot of  $n$  against  $\Delta\Omega_1$ , the product of all the free parameters of Eq. 2.4 can be obtained.

The activity of the source ( $S$ ) was calculated starting from an old certified value (see Sec. 2.1), while the branching ratio ( $BR$ ), whose value is 99.944%, was found in the scientific literature.

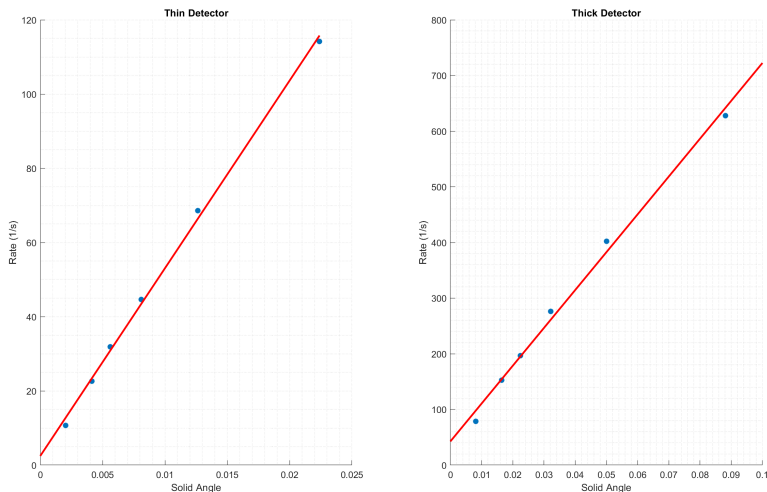


Figure 2.24: *Rate versus solid angle both for thin and thick scintillators.*

The collected spectra were fitted with a suitable function, specifically a sum of a gaussian function for the peak and an exponential one for the background. Since the rate is:

$$n = \frac{I}{\Delta t}$$

where  $\Delta t$  is the measure time, which was kept the same for every spectrum (10 minutes), and  $I$  is the total number of detected events. The latter ( $I$ )

was found by calculating the area of the gaussian fit of the peak, considering that the area subtended by a gaussian function  $G(A, \mu, \sigma)$  is given by:

$$I = \sqrt{2\pi}\sigma A$$

where  $A$  is the amplitude and  $\sigma$  is the variance.

The solid angle  $\Delta\Omega$  was then calculated at the different distances, using the formula for a cylindrical detector of radius  $a$ , at a distance  $d$  from the source, which is the following:

$$\Delta\Omega = 2\pi \left(1 - \frac{d}{\sqrt{d^2 + a^2}}\right) \quad (2.5)$$

Having all the necessary quantities, it was possible to obtain a linear fit rate versus solid angle. In Fig. 2.24 the plot of the rate against the solid angle for both scintillators is shown.

Extrapolating two angular coefficients from the two linear fits in Fig. 2.24, it was possible to obtain efficiencies.

From Eq. 2.4, the angular coefficient ( $m$ ) of the linear fit is:

$$m = \frac{\epsilon \cdot 2S \cdot BR}{4\pi} \quad (2.6)$$

By inverting the Eq. 2.6:

$$\epsilon = \frac{m \cdot 4\pi}{2S \cdot BR}$$

The resulting efficiencies, with their own statistical uncertainty, were  $\epsilon_1 = 0.16 \pm 0.01$  and  $\epsilon_2 = 0.22 \pm 0.02$ . Uncertainty on the solid angle values was computed with the well known error propagation formulas, taking 2 mm of uncertainty on the measured distances. In the same way, uncertainty on the detection rate was obtained by propagating those of the parameters of the gaussian function (given by the fit) into the formula of the area of the peak, and considering neglectable the uncertainty of the measurement time ( $\approx 1ms/600s$ ). Extrapolating the error of the angular coefficient from linear fit with a confidence interval of 95%, the error on the efficiencies was obtained.

## 2.8 Temperature fluctuations and peak derive

Like all circuits, those belonging to the acquisition chain, such as amplifiers, PMTs and discriminators, have an optimal working temperature. This temperature was reached several days after switching the electronics on, but it was not constant during the day nor during the week and not even during the months. In fact, the electronics are not isolated from the air of the laboratory which is not thermostated. So, it was necessary to check whether the

the electronics were stable under variable conditions and, therefore, trying to decouple the experimental results from the environmental conditions.

To verify this, it was decided to follow the position of the peak at 511 keV energy over time and see which channels the average value fell into. Thanks to an automatically running program with MAESTRO, a value of the position of the peak was collected at equally spaced intervals in time for about twenty days. To do this, it was necessary to turn off the case with all the electronics to cool the circuits and, after a few days, to turn the system on again in order to start the measurements.

Assuming that the achievement of the equilibrium temperature would have followed an exponential law, the time intervals in the first days were chosen shorter (both acquisition time and time interval between two consecutive measurements) and, therefore, the results are closer to each other, aiming to obtain a better characterization of the ignition curve.

Looking at the graph in Fig. 2.25, it can be seen how the position of the peak moves itself over time along the plot in the channels of the MCA. This time drifting must be taken into consideration if it's necessary to calibrate the detector on an energy scale.

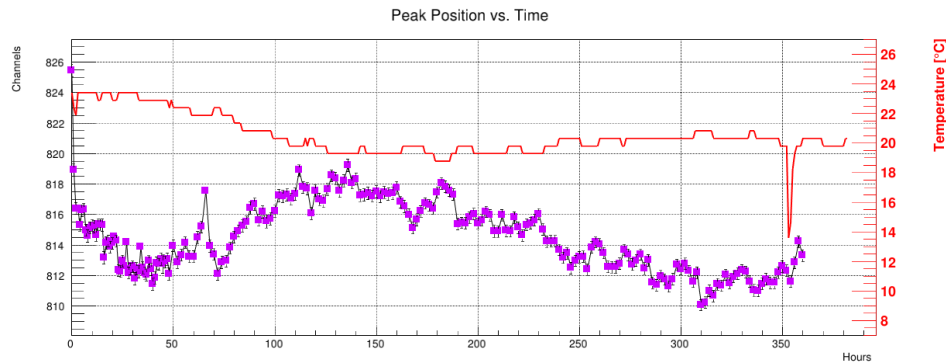


Figure 2.25: *Change in peak position due to the 511 keV range over time. The air temperature trend in the laboratory is shown in red.*

Furthermore, in every measurement, this systematic error should be added to the statistical one. For this reason, the error associated with the position of the peak was averaged once the temperature had reached its equilibrium value.

As expected, the uncertainty related to the environmental conditions can be considered neglectable when compared with the other source of error discussed in the next sections. *E.g.* in Sec. 2.9 it will be shown that the finite dimensions of the scintillators and the target introduced an uncertainty on the scattering angle, and so on the detected energy, which was comparable with the resolution of the spectrometer (about 8%). It is much more relevant than the one given by the thermal drift of the peak position.

Indeed, as can be seen in Fig. 2.25, the RMS (Root Mean Square) of this drift can be approximately estimated to amount to 4-5 channels, while an 8% FWHM corresponds to roughly 80 channels (for spectroscopy measurements a 1024 channels binning was chosen).

Furthermore, each of the spectra acquired over the twenty days was fitted to extrapolate the width of the peak (*i.e.* the  $\sigma$  parameter of the gaussian fit function) and, consequently, the resolution of the experimental apparatus (*i.e.*  $FWHM \approx 2.35 \cdot \sigma$ ). The plot of the time evolution of the peak width is shown in Fig. 2.26: as can be seen, after a certain period, the width does not substantially change from a value approximately equal to 28.5 channels, that gives a value (in channels) of the FWHM equal to:

$$FWHM = 2.35 \cdot 28.5 \approx 67.0$$

And so, taking an arithmetic average of the peak position values plotted in graph 2.25, the resolution resulted to be:

$$R = \frac{67.0}{820.3} \approx 0.08$$

So it does not significantly differ from the value calculated in Sec. 2.3.

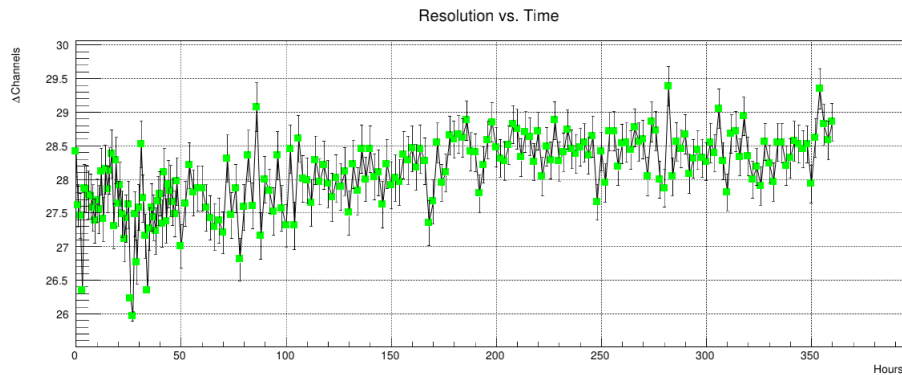


Figure 2.26: Variation in peak width as a function of temperature that changes over time.

## 2.9 Geometrical setup

The experimental setup in Fig. 2.27 was arranged to perform the measurements to verify Compton Law (Sec. 3.2) and Klein-Nishina formula (Sec. 3.3). The scattering target was placed at the centre of the setup, with the sodium source between it and the 2" detector (A in Fig. 2.27). In order both to detect photons scattered at a certain angle and to measure their energy, 1" scintillator was rotated and pointed toward the target. For a given angle  $\theta$ , the target was also rotated of angle  $\frac{\theta}{2}$ , in order to minimize the photon

absorption in the material. Two different configurations were used: reflection and transmission, both described in detail in the next section. Distances between all the components were chosen in order to optimize both energy resolution and detection efficiency. These choices are briefly discussed and justified in this paragraph. Firstly, the finite transversal section of the detectors obviously implies an uncertainty on the scattering angle of the detected photons. The energy of the scattered photons is given by Eq. 1.1, which, for  $h\nu = m_e c^2$ , reduces to:

$$E(\theta) = h\nu' = \frac{h\nu}{2 - \cos \theta} \quad (2.7)$$

Through the propagation of the angle uncertainty  $\Delta\theta$  on the energy value, the following equation for energy relative uncertainty was found:

$$\frac{\Delta E}{E} = \frac{1}{E} \cdot \frac{dE}{d\theta} \cdot \Delta\theta = -\frac{\sin \theta}{(2 - \cos \theta)^2} \cdot \Delta\theta \quad (2.8)$$

The resulting expression was imposed to be smaller than the resolution ( $R$ ) of the 1" scintillator (B in Fig. 2.27), the one used for spectroscopy, which was about 8% (see Sec. 2.3). This was done in order to avoid that the uncertainty on the scattering angle could introduce an uncertainty on the measured energy bigger than the one given by the resolution of the spectrometer. This constraint imposed various conditions, which are fully described below, on all the distances shown in Fig. 2.27:  $d_{AS}$  (2" detector-source),  $d_{SC}$  (source-target) and  $d_{BC}$  (target-1" detector).

Photons detected by the gate scintillator are just those moving in the solid angle spanned by its surface. So their incidence angle  $\Delta\theta_1$  can vary between 0 and  $\Delta\theta_1$  (see Fig. 2.27), which is simply:

$$\Delta\theta_1 = \arctan \frac{r_A}{d_{AS}}$$

where  $r_A$  is the radius of the circular surface of the gate scintillator.

If a photon incide on the gate detector with  $\Delta\theta_1$ , the other one, emitted back-to-back, incides on the target with  $\Delta\theta_1$  too. Here, in the worst case, it can undergo scattering Compton of angle  $\Theta$  (in red in Fig. 2.27) and then be detected by 1" scintillator as a photon scattered at  $\theta$  (the rotation angle of the detector B).

So, the resulting error on the angle, which is the maximum possible in this setup, is:

$$\Delta\theta = \Theta - \theta = \Delta\theta_1 + \Delta\theta_2$$

Since:

$$\Delta\theta_1 = \arctan \frac{r_A}{d_{AS}} \quad \text{and} \quad \Delta\theta_2 = \arctan \frac{r_B}{d_{BC}}$$

where  $r_A$  and  $r_B$  are the radius of the 2" and 1" detectors while  $d_{AS}$  and  $d_{BC}$  are the distances between the source and the 2" and 1" detectors respectively.

At the end, being  $r_B \ll d_{BC}$  and  $r_2 \ll d_{AS}$ , it was obtained:

$$\Delta\theta \approx \frac{r_A}{d_{AS}} + \frac{r_B}{d_{BC}} \quad (2.9)$$

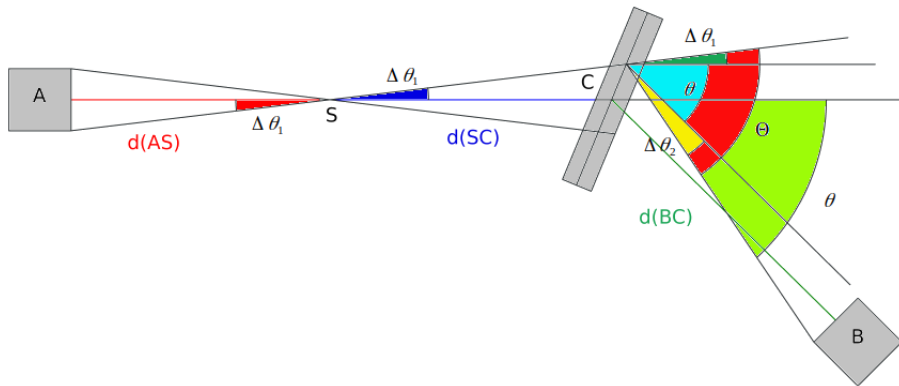


Figure 2.27: 2D Geometrical setup for the spectroscopy measurements.

Then, it can be proved that, from Eq. 2.8,  $|\frac{1}{E} \cdot \frac{dE}{d\theta}|$  has a maximum equal to  $1/\sqrt{3}$  at  $\theta = \pi/3$ . Recalling the previously mentioned constraint, ( $\Delta E/E \leq$  resolution R), the following inequality was enforced:

$$\underline{\Delta\theta \leq R \cdot \sqrt{3} \approx 0.14} \quad (2.10)$$

So, being  $r_B = 0.5' \approx 1.27$  cm,  $r_A = 1' \approx 2.54$  cm and assuming  $d_{AS} = d_{BC}$ , from Eq. 2.9:

$$d_{AS} = d_{BC} \approx \frac{r_A + r_B}{\Delta\theta} \geq 27.21 \text{ cm}$$

So  $d_{AS} = d_{BC} = 28$  cm were chosen in order to satisfy Eq. 2.10.  $d_{SC}$  was chosen equal to 28 cm too.

A target placed too far from the source would not be indeed reached by the same flux of photons incident on the gate detector, so reducing the interaction rate. On the other side, a too close setting would expose a smaller surface of the target to the effective flux of photons, i.e. flux of photons corresponding to the ones detected by the gate. These photons are the only interesting ones, since the others do not trigger the gate system. If they incide on a small fraction of the target surface only, they will interact just with an equally reduced fraction of the medium electrons: therefore detection efficiency will be lowered in this case too. A 3D scheme of the geometrical setup is shown in Fig. 2.28.

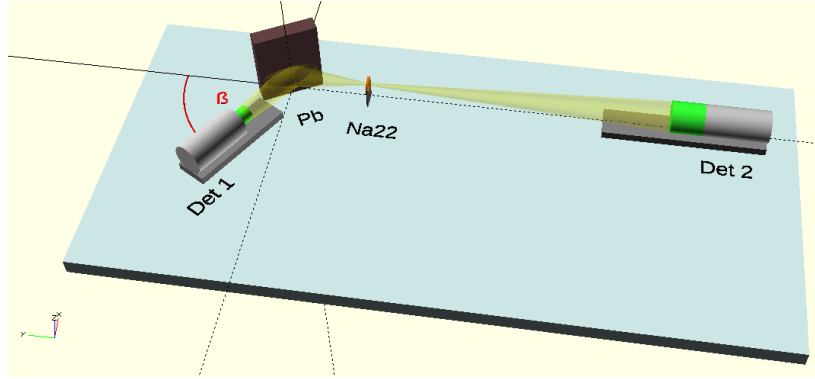


Figure 2.28: 3D Geometrical setup for the spettroscopy measurements.

## 2.10 Probability of interaction

One of the main aspects to consider is the thickness of the scatterer itself ( $D$ , see Fig. 2.29) in order to evaluate and then optimize the probability of interaction of the photons in the target. As already mentioned, measurements were performed in two different configurations:

- Reflection, in which a photon, after being Compton scattered at a certain depth  $x$ , must go back through a same length path in the medium, as can be seen in Fig. 2.29. Reflection mode is obviously the only one useful for scattering angles  $\frac{\pi}{2} \leq \theta \leq \pi$ .
- Trasmission, in which the scattered photon's path ( $D' - x$ ) is in general different from that of the incident one ( $x$ ). In this case, a too thick scatterer would likely absorb too many of the beam photons, drastically reducing the rate of the Compton interaction. On the other side, a too thin one would not obviously provide enough electrons to achieve a good interaction rate.

The number of photons scattered while crossing the infinitesimal thickness of the target ( $x, x + dx$ ), which are detected by the 1" scintillator at an angle  $\theta$ , can be computed through the following equation:

$$dn = n(2) N_e \frac{d\sigma}{d\Omega_B} \Delta\Omega_B \epsilon(1, E') f(x, D, \theta) dx \quad (2.11)$$

Note that, as it can be seen in Fig. 2.27, the 1" scintillator is called B while the 2" scintillator is called A. Where:

- $N_e$  is the number of target electrons defined as  $N = \rho N_A \frac{Z}{A}$  ( $\rho$  is the density of the material,  $Z$  its atomic number and  $A$  its atomic mass);
- $\frac{d\sigma}{d\Omega}$  is the differential Compton cross section;

- $\Delta\Omega_{A/B}$  are the solid angles spanned by the two detectors;
- $\epsilon(1, E')$  is the efficiency of the spectrometer scintillator that depends on the energy of the scattered photon;
- $f(x, D, \theta)$  is instead the attenuation function for a beam of photons interacting in the target after a path  $x$  inside it;
- $n(2)$  is the number of photons detected by the gate scintillator, which corresponds to:

$$n(2) = 2S \cdot BR \cdot \epsilon(2, E) \frac{\Delta\Omega_A}{4\pi}$$

where  $S$  is the activity of the source,  $BR$  is the branching ratio of  $^{22}\text{Na}$   $\beta^+$  decay and  $\epsilon(2, E)$  is the peak efficiency of the gate scintillator.

Evaluation of this function was performed as follows.

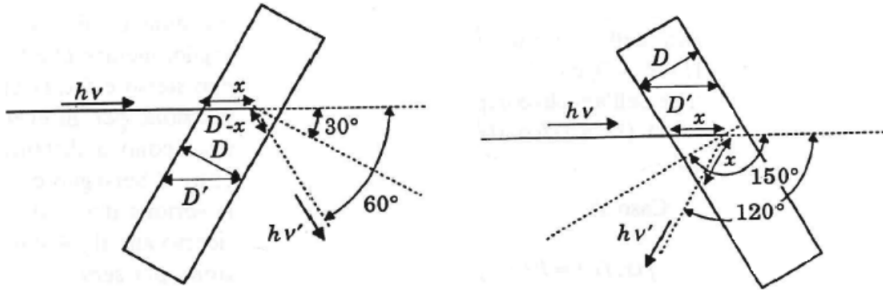


Figure 2.29: Photon in the scatterer medium both in transmission (left) and in reflection (right).

Firstly, recall the definition of  $\lambda$ , the attenuation length of the crossed material:

$$\lambda \equiv \frac{1}{\mu} \quad (2.12)$$

where  $\mu$  is the absorption coefficient.

Let then  $P(x, \lambda)$  be the probability that a photon of energy  $E$  does not interact after crossing a thickness  $x$  in a medium of attenuation length  $\lambda = \lambda(E)$ . Similarly, let  $P(D' - x, \lambda')$  be the probability for the scattered photon of energy  $E'$  not to interact in the remaining path  $D' - x$  in the same medium, whose attenuation length  $\lambda'$  has obviously changed with energy after the interaction.

For transmission setup in Fig. 2.29 (left):

$$D' = \frac{D}{\cos(\theta/2)}$$

Then, the attenuation function can be written as:

$$f(x, D, \theta) = f(x, D') = P(x, \lambda) \cdot P(D' - x, \lambda')$$

Interaction probabilities can be easily computed remembering that the number of photons ( $N$ ) of a beam crossing a material follows an exponential law. Any possible interaction (photoelectric effect, Compton scattering and, if energetically possible, pair production) subtract a quantum from the beam, either absorbing or scattering it. So, recalling Eq.2.12, the amount of photons lost crossing a path  $dx$  is:

$$dN = -N\mu dx = -\frac{N}{\lambda}dx$$

and so, being  $N_0$  the initial number of photons, the result is

$$N(x) = N_0 \cdot e^{-x/\lambda}$$

Probability of not interacting after  $x$ , i.e.  $P(x, \lambda)$  is just  $e^{-x/\lambda}$ , and equally  $P(D' - x, \lambda')$  is  $e^{-(D-x')/\lambda'}$ . So, the expression for the attenuation function is finally derived:

$$f(x, D, \theta) = e^{-x/\lambda} \cdot e^{-(D-x')/\lambda'}$$

Defining now  $\mu_C$ , whose dimensions are the same of that of an absorption coefficient, as

$$\mu_C \equiv N_e \frac{d\sigma}{d\Omega_B} d\Omega_B.$$

Eq. 2.11 now can be finally rewritten as

$$dn = n(2) \epsilon(1, E') \mu_C e^{-x/\lambda} e^{-(D-x')/\lambda'} dx \quad (2.13)$$

Then, the total amount of photons detected by the 1" scintillator (B), which are those that succeeded in completely crossing the material, can be found integrating Eq.2.13 from 0 to  $D'$ :

$$\begin{aligned} \Delta n_1 &= n(2) \mu_C \epsilon(1, E') \int_0^{D'} e^{-x/\lambda} \cdot e^{-(D-x')/\lambda'} dx = \\ &= n(2) \epsilon(1, E') \mu_C K_1 \end{aligned} \quad (2.14)$$

where

$$K_1 \equiv \int_0^{D'} e^{-x/\lambda} \cdot e^{-(D-x')/\lambda'} dx$$

A similar calculation for the reflection setup can be proved:

$$\Delta n_2 = n(2) \cdot \epsilon(1, E') \mu_C K_2 \quad (2.15)$$

In this case, the distance the photon has to travel to exit the target is the same traveled to get to the interaction point, which is  $x$ . So, the probability of exit without any further interaction is just  $e^{-x/\lambda'}$  and so

$$K_2 \equiv \int_0^{D'} e^{-x/\lambda} \cdot e^{-x/\lambda'} dx$$

The evaluation of these integrals above gives the following results:

$$K_1 = \lambda_1 e^{-D'/\lambda} (1 - e^{-D'/\lambda_1}) \quad \text{with} \quad \lambda_1 = \frac{\lambda \cdot \lambda'}{\lambda' - \lambda}$$

$$K_2 = \lambda_2 (1 - e^{-D'/\lambda_2}) \quad \text{with} \quad \lambda_2 = \frac{\lambda \cdot \lambda'}{\lambda + \lambda'}$$

<b>Angle</b> $\theta$	<b>Energy</b> [keV]	<b>Copper</b> ( $\rho=8.96 \text{ g/cm}^3$ ) [ $\lambda\rho = 12 \text{ g/cm}^2$ $D = 1.7 \text{ cm}$ ]				<b>Lead</b> ( $\rho=11.34 \text{ g/cm}^3$ ) [ $\lambda\rho = 6.2 \text{ g/cm}^2$ $D = 0.6 \text{ cm}$ ]			
		<b>D'</b> [cm]	$\lambda'\rho$ [g/cm <sup>2</sup> ]	$K_1$ [cm]	$K_2$ [cm]	<b>D'</b> [cm]	$\lambda'\rho$ [g/cm <sup>2</sup> ]	$K_1$ [cm]	$K_2$ [cm]
0°	511	1.70		0.165	0.60			0.048	
10°	503.3	1.71		0.166	0.60			0.48	
15°	494.2	1.72	12	$-\infty$	0.167	0.61	6.2	$-\infty$	0.049
20°	481.9	1.73		0.168	0.61			0.049	
30°	450.6	1.76		0.170	0.62			0.050	
40°	414.1	1.81		0.175	0.173	0.64		0.052	0.050
45°	395.2	1.85	10.6	0.179	0.176	0.65	4,3	0.053	0.050
50°	376.5	1.88		0.181	0.178	0.66		0.054	0.051
55°	358.2	1.91		0.184	0.181	0.68		0.055	0.052
60°	340.7	1.96		0.191	0.182	0.69		0.059	0.050
65°	323.9	2.03		0.197	0.187	0.71		0.060	0.052
75°	293.5	2.16	8.9	0.208	0.196	0.76	2.5	0.065	0.055
80°	279.8	2.22		0.213	0.201	0.78		0.067	0.056
90°	255.5	2.40		0.227	0.214	0.85		0.072	0.060
120°	204.4	3.40	6.4	-	0.260	1.20	0.1	-	0.089
140°	184.7	4.97		-	0.325	1.75		-	0.089

Table 2.5:  $K_1$  (trasmission) and  $K_2$  (reflection) coefficient values for copper and lead targets. The values of  $\lambda'$  were taken from NIST database.

As can be easily seen by looking at Eq. 2.14 and Eq. 2.15, in order to maximize the rate of detected events ( $\Delta n_1$  and  $\Delta n_2$ ), it's necessary to maximize  $K_1$  and  $K_2$ .  $K_1$  has a maximum for a finite value of  $D$ , while  $K_2$  increases with  $D$ , asymptotically reaching  $\lambda_2$ . Indeed:

$$K_1^{max} = \lambda \frac{\lambda'}{\lambda} \left( 1 - e^{-\frac{\lambda}{\lambda' - \lambda}} \right) \quad for \quad D_{max} = \lambda_1 \log \left( \frac{\lambda'}{\lambda} \right) \cos \left( \frac{\theta}{2} \right)$$

$$K_2^{max} \rightarrow \lambda_2 \quad for \quad D \rightarrow \infty \quad (2.16)$$

In the measurements performed to verify Klein-Nishina formula, the thickness of the copper target used was  $D = 1.6$  cm. In fact, to perform the measurements in reflection mode, the target had to be as thick as possible, as prescribed by Eq. 2.16. For what concerns transmission configuration, calculations gave  $D_{max} \approx 2.0$  cm, so the performed choice was justified in this case too. So the thickest copper targets were chosen among the few available in the laboratory. For this target,  $K_1$  and  $K_2$  values at different angles are listed in Tab.2.10, together with those for a 0.6 cm lead target, which was then discarded as it did not provide a sufficiently high statistics.

# Chapter 3

## Data analysis

This chapter presents the main results obtained in the experiment, while the in-depth analysis and some tricks have been reported in the appendix. It must be emphasized that after calculating the best adjustment to have sufficiently high statistics, as shown in the previous chapter, it was decided to switch from a binnage of 8192 channels, or voltage intervals, to, firstly, a binning of 2048 and then one of 1024. The error associated with the change of scale was considered negligible as explained in the appendix.

### 3.1 Background

Aiming to minimize the background signals from environmental radiation, a passive shielding was set up using some lead bricks, together with the active one described in details in Sec. 2.5. Furthermore, to extrapolate the parameters of interest from the measured signals, the remaining background was subtracted from the spectra with an exponential function. In fact, data were fitted with the following parametric function:

$$f(x) = p[0] + e^{p[1]+p[2]\cdot x} + p[3]e^{-\frac{1}{2}\frac{(x-p[4])^2}{p[5]^2}} \quad (3.1)$$

As it can be seen in Fig. 3.1, over 200 keV, it results that the peak grows on a decreasing exponential type curve and, consequently, the fit adapts itself perfectly to the measured experimental values. Other types of background were assumed, such as the linear or the parabolic, as well as the error function-like ones. However, basing on  $\chi^2$ , the exponential one was the most suitable.

On the other hand, under the energy of 200 keV, the background was estimated to be parabolic or a higher order polynomial. However, the angles for which the peak occurs at an energy lower than 200 keV are only the few highest ones. An alternative method to perform background subtraction is to take a counting measurement without any source for a few days and normalize it for the measurement time. By doing so, it is possible to obtain an

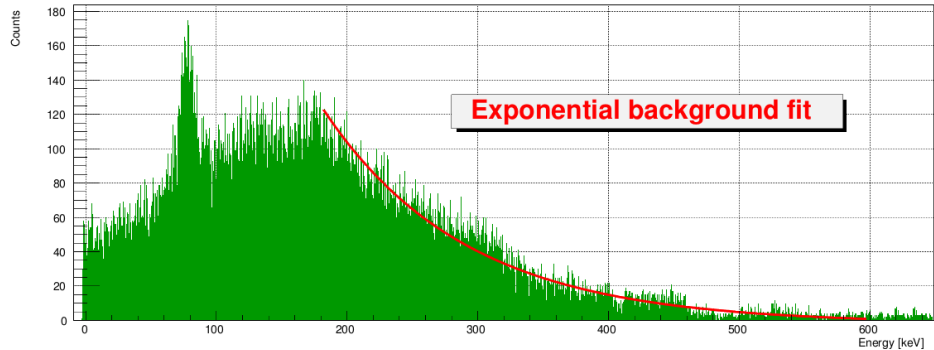


Figure 3.1: *Measurement of a spectrum without a source used as a verification of the correct assumption of the shape of the background.*

estimation of the environmental background contribution to be subtracted from all the spectra.

Since a subtraction of the background bin by bin would have left a spectrum that would still have to be fitted with a "signal + background" function, so the first fit method was chosen.

The background was subtracted by using the function defined in Eq. 3.1 while the direct background measurement was then used as a comparison to explain the presence of some characteristic environmental peaks in the spectrum, as it can be seen from the spectrum in Fig. 3.1.

## 3.2 Compton Law

The aim of this section is the experimental proof of the Compton Law that has been already mentioned in Sec. 1.1. The formula is rewritten below (Eq. 1.1).

$$h\nu' = \frac{h\nu}{1 + \frac{h\nu}{m_0 c^2} (1 - \cos \theta)}$$

where  $h\nu'$  is the final energy of the scattered photon,  $h\nu$  is the initial energy of the photon (511 keV),  $\theta$  is the scattering angle and  $m_0$  is the electron rest mass, therefore the value of  $m_0 c^2$  is equal to 511 keV.

By measuring the energy of photons scattered at different angles, ( $\theta$ ) it is possible to prove the Compton formula. For this part of the experiment, the coincidence mode with the gate scintillator was used. In the process, the 511 keV photon incides on the scatterer, which is rotated of a certain angle, ( $\theta/2$ , so half of the scattering one) to maximize the detection, then changes its direction and, finally, is detected by the thinnest scintillator, placed at a chosen angle ( $\theta$ ). Four example of different spectra at four different angles are shown in Fig. 3.2.

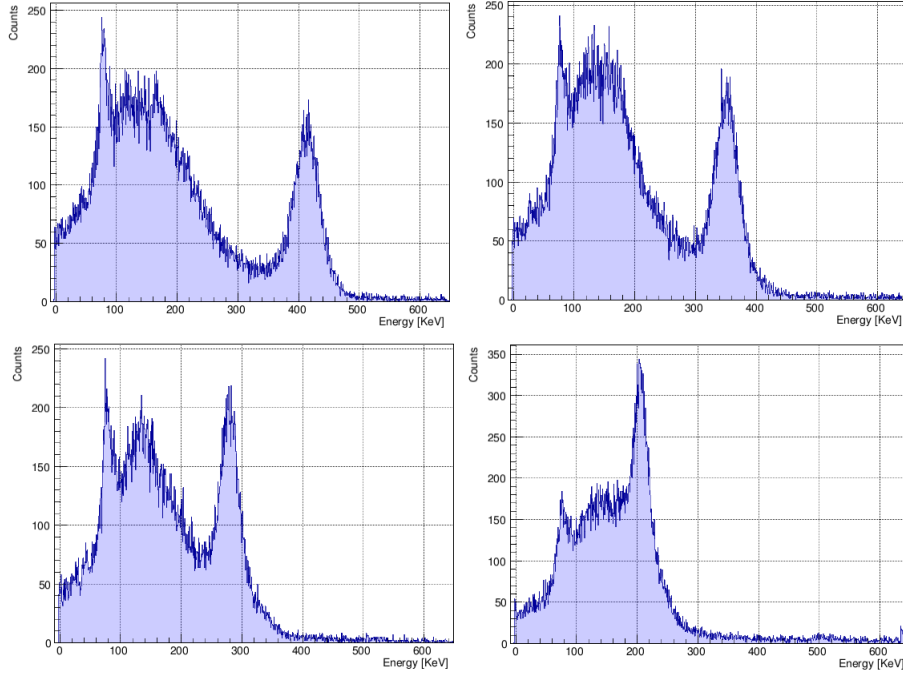


Figure 3.2: *Cu spectra at four different angles:  $\theta = 25^\circ$  (on the top left)  $\theta = 55^\circ$  (on the top right)  $\theta = 80^\circ$  (on the bottom left)  $\theta = 120^\circ$  (on the bottom right).*

It can be noticed that the more the angle ( $\theta$ ) increases the more the 511 keV peak moves itself on the left side along the spectrum. Indeed energy of the scattered photon decreases with increasing the angle, as prescribed by Compton Law (Eq. 1.1)

The analysis regards two different materials, which were used as scattering target: copper (Cu) and lead (Pb), both in transmission and in reflection (see Sec. 2.10) Angles in transmission and reflection, for copper and lead, are listed in Tab. 3.2 and Tab. 3.1.

First, a conversion from ADC spectrum to energy spectrum by the energy calibration was made (Sec. 2.6). Then, after the scattered photon peak was fitted with a gaussian function, the mean of the gaussian was extrapolated, obtaining the energy of the Compton peak at a specific angle.

Tab. 3.2 and Tab. 3.1 summarized the obtained results, where the expected energy was computed using Eq. 1.1.

The error of the gaussian mean too ( $\delta_E$ ) was extrapolated from the gaussian fit of the peak.

Angle $\theta$	Expected Energy[KeV]	Measured Energy[KeV]	$\delta_E$
0°	511.000	514.221	0.48238
10° (ref)	503.352	510.791	3.58522
10°	503.352	497.681	1.74588
15° (ref)	494.160	491.700	11.4988
15°	494.160	499.381	0.48685
20° (ref)	481.935	498.729	0.67045
30° (ref)	450.627	480.259	0.43440
50°	376.507	371.098	0.54697
90° (ref)	255.500	254.119	0.76676

Table 3.1: Selected angles, Expected Energy and Measured Energy with its error ( $\delta_E$ ) for the experimental proof of Compton formula with Pb scatter.

Angle $\theta$	Expected Energy[KeV]	Measured Energy[KeV]	$\delta_E$
Compton with Cu Scatter (Transmission).			
0°	511.000	507.562	0.49834
15°	494.161	486.184	0.35177
30°	450.627	435.836	0.79922
45°	395.237	387.055	0.59863
60°	340.666	338.727	0.39892
75°	293.478	291.358	0.46627
90°	255.500	259.270	0.37138
Compton with Cu Scatter (Reflection).			
10°	503.352	497.041	2.54e-05
20°	481.935	481.843	4.77413
25°	467.224	463.361	0.70646
40°	414.115	413.509	0.26474
50°	376.507	367.116	0.69926
55°	358.238	351.239	0.25165
65°	323.954	325.735	0.30098
80°	279.792	272.584	0.24924
120°	204.400	206.158	0.22330
140°	184.740	186.143	0.17440

Table 3.2: Selected angles, Expected Energy and Measured Energy with its error ( $\delta_E$ ) for the experimental proof of Compton formula with Cu scatter.

Plotting angles versus measured energy, the data were fitted with Eq. 1.1 keeping  $h\nu$  and  $m_0c^2$  as free parameters. Fig. 3.3 and Fig. 3.4 show the obtained data for copper and lead with two fits: one for transmission angles and the other for reflection angles related to the theoretical function, which was obtained using the expected value of  $m_0c^2 = E_0 = 511$  keV. Error on the measured energy, obtained from the gaussian fit of the peak, and the error on the angles, assumed to be around  $2^\circ$ , were both added to those plots.

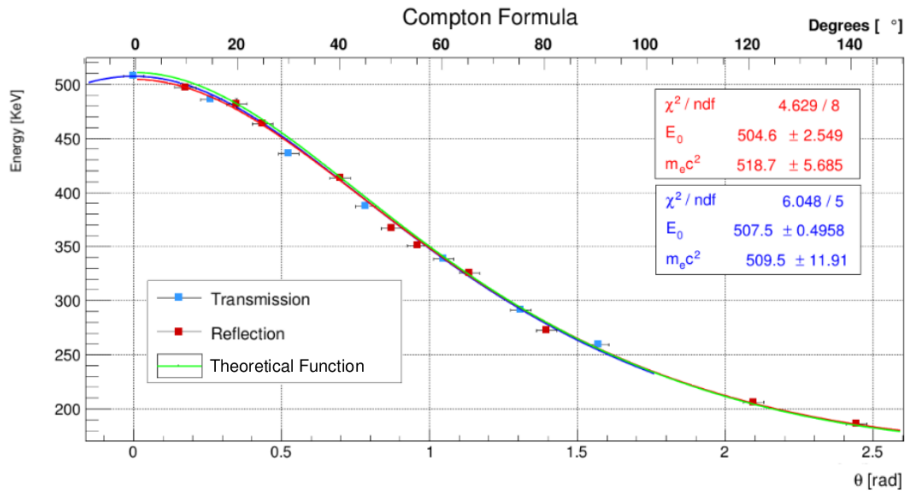


Figure 3.3: Cu data with a fit for transmission angles (blue), a fit for reflection angles (red) and the theoretical Compton formula (green).

The free parameters ( $h\nu$  and  $m_0c^2$ ) with their errors obtained from the fit are summarized in Tab. 3.3. The distance in  $\sigma$  for each parameter of the measured value from the theoretical one (511 keV) was computed in order to estimate the goodness of the parameters. The following formula was used:

$$t = \frac{|x_m - x_{th}|}{\sigma} \quad (3.2)$$

where  $t$  is the distance in  $\sigma$ ,  $x_m$  is the measured value,  $x_{th}$  is the theoretical value which is obviously 511 keV and  $\sigma$  is the error associated with the measured value.

From the transmission measurements, both for copper and for lead, the  $h\nu$  parameter was estimated and it differed from the true value by several sigma. This is due to the fact that the estimation of the error of the parameter is very small, although  $\chi^2$  value did not result in an underestimation of the errors associated with the measurements. A possible explanation is the neglection of some systematic error.

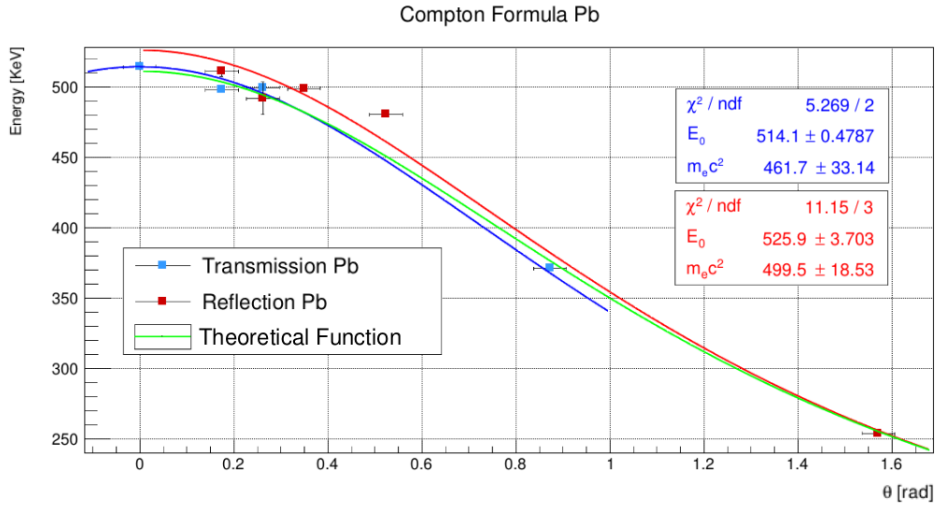


Figure 3.4: *Pb data with a fit for transmission angles (blue), a fit for reflection angles (red) and the theoretical Compton formula (green).*

Material		Free Parameter	Value [keV]	$\delta_E$ [keV]	$t[\sigma]$
Copper	Transmission	$h\nu$	507.5	0.5	7
		$m_0 c^2$	509.5	11.9	0.13
	Reflection	$h\nu$	504.6	2.5	2.56
		$m_0 c^2$	518.7	5.7	1.35
Lead	Transmission	$h\nu$	514.1	0.5	6.2
		$m_0 c^2$	461.7	33.1	1.49
	Reflection	$h\nu$	525.9	3.7	4.03
		$m_0 c^2$	499.5	18.5	0.62

Table 3.3: *Free parameters extrapolated from the Compton fit and their distance in  $\sigma$  from the theoretical value.*

### 3.3 Klein-Nishina differential cross section

As previously shown in the Sec. 1.2, angular distribution of Compton-scattered unpolarized photons can be computed using the Klein-Nishina formula for differential cross section (Eq. 1.5).

$$\frac{d\sigma}{d\Omega} = \frac{Z}{2} r_0^2 \left( \frac{1 + \cos^2 \theta}{1 + \alpha(1 - \cos \theta)} \right) \cdot \left( 1 + \frac{\alpha^2(1 - \cos \theta)^2}{(1 + \cos^2 \theta)[1 + \alpha(1 - \cos \theta)]} \right)$$

Since scattered photons come from positronium annihilation,  $\alpha = E/m_e = 1$ , so the formula reduces to:

$$\frac{d\sigma}{d\Omega} = Zr_0^2 \left( \frac{3 - \cos \theta + 3 \cos^2 \theta - \cos^3 \theta}{(2 - \cos \theta)^3} \right) \quad (3.3)$$

The second goal of this experiment was the verification of this formula and the estimation of the parameter  $r_0$  (the classical radius of the electron). To achieve it, in order to estimate the differential cross section, it was related to the rate of Compton interaction, keeping into account the finite efficiency of the measurement system too. The differential cross section of a scattering process is, by definition:

$$\frac{d\sigma}{d\Omega} = \frac{1}{F} \frac{d^2N}{dt d\Omega} \quad (3.4)$$

where  $\frac{d^2N}{dt d\Omega}$  is the rate of scattered particles per unit time and solid angle and  $F$  the incoming flux. Recalling Eq. 2.14 and Eq. 2.15, the previous expression can be rewritten as:

$$\frac{d\sigma}{d\Omega} = \frac{\Delta n}{2S \cdot BR \cdot \epsilon_A \cdot \frac{\Delta\Omega_A}{4\pi} \cdot d\Omega_B \cdot \epsilon_B \cdot N_e \cdot K(E')} \quad (3.5)$$

The rate  $\Delta n$  was calculated just as  $\Delta n = \frac{I}{\Delta t}$ , where  $I$  is given by the area under the gaussian fit function and  $\Delta t$  is the acquisition time. All the parameters appearing in Eq. 3.5 contribute to the total uncertainty on the differential cross section evaluation (except for branching ratio, which is known with a precision of order  $10^{-4}$ ).

The statistical uncertainty on the incoming rate was computed, as previously done in Sec. 2.7, considering neglectable the uncertainty on acquisition time and calculating that on the number of detected events starting from the formula:

$$I = \sqrt{2\pi}\sigma A$$

The uncertainty on the area was then found using error propagation formulas, taking  $\sigma_A$  and  $\sigma_\sigma$  from the fit results.

Uncertainty on the solid angles  $\Delta\Omega_1$  and  $\Delta\Omega_2$  were computed using formula in Eq. 2.5 and assuming an error of 1 mm on the distance measure, while those on the efficiencies of the two detectors were already evaluated in Sec. 2.1. Uncertainty on the activity of the source was evaluated in Sec. 2.1.1 and is equal to  $\sigma_S = 0.6$  kBq.

Different spectra, whose an example is reported in Fig. 3.2 , were collected varying the angle, using the same coincidence setup as for the spectroscopy experiment and a copper target of  $5 \text{ cm} \times 5 \text{ cm} \times 0.6 \text{ cm}$ , working in reflection mode for  $\theta=\{40^\circ, 55^\circ, 65^\circ, 80^\circ\}$ , and in transmission for  $\theta=\{15^\circ, 45^\circ, 60^\circ, 75^\circ, 90^\circ\}$ .

Collection time was roughly the same for every spectrum (about one week) to provide high enough statistics also for high-angle scatterings, expected to be less probable (Eq. 3.3). In Tab. 3.4 for each sampled angle different results are shown, including scattering rate, measured and expected differential cross section and their difference, expressed in terms of the variable  $t$  defined in Eq. 3.2. In the table  $\Gamma \equiv \frac{d\sigma}{d\Omega}$ .

Angle $\theta$	Area	$t_{mis}$	Rate	$\Gamma$	$\sigma_\Gamma$	Expected $\Gamma$	$t[\sigma]$
		[s]	[Hz]	[cm <sup>2</sup> ]	[cm <sup>2</sup> ]		
15°	9068.6	167938	0.054	1.670e-24	0.112e-24	2.056e-24	3.51
40°	10370.3	420851	0.025	9.942e-25	0.065e-24	1.217e-24	3.44
45°	6967.8	162042	0.043	1.333e-24	0.086e-24	1.065e-24	3.11
55°	10546.5	420441	0.025	1.012e-24	0.066e-24	8.137e-25	3.00
60°	8610.0	410000	0.021	6.403e-25	0.041e-24	7.157e-25	1.84
65°	6851.82	431315	0.016	6.412e-25	0.042e-24	6.350e-25	0.14
75°	7516.8	417600	0.018	5.476e-25	0.036e-24	5.183e-25	0.79
80°	8004.35	419017	0.020	7.695e-25	0.051e-24	4.785e-25	5.69
90°	8447.2	603374	0.014	4.212e-25	0.028e-24	4.263e-25	0.18

Table 3.4: Summary of all the experimental results obtained for the calculation of the Klein-Nishina cross section with the relative error and distance from the expected value in  $\sigma$  units ( $t$ ).

Collected data were then fitted with the function of the scattering angle  $\theta$  defined in Eq. 3.3. Uncertainty on scattering angle was assumed to be of 2°. This fit is shown in Fig. 3.5. The only free parameter of the fit is the classical radius of the electron, whose best estimation and uncertainty were obtained:

$$r_0 = (2.78 \pm 0.09) \cdot 10^{-13} \text{ cm}$$

The experimental result is fully compatible with the expected one,  $r_0 \approx 2.817 \cdot 10^{-13} \text{ cm}$ .

Indeed

$$t = \frac{|r_0^{mes} - r_0^{exp}|}{\sigma_{r_0}} = 0.375$$

and so  $p_{value} \approx 0.34 > 0.05$ .

Experimental data points of measured  $\frac{d\sigma}{d\Omega}$  together with the theoretical expected shape of the Klein-Nishina differential cross section for 511 keV photons are shown in Fig. 3.6 in polar coordinates. Note that Klein-Nishina formula is indeed invariant under  $\theta \rightarrow -\theta$ .

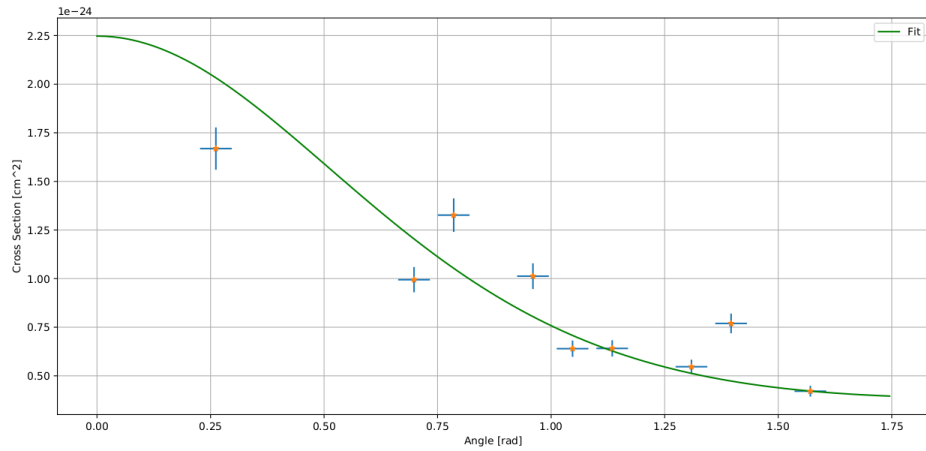


Figure 3.5: *Experimental data of the Klein-Nishina cross section at various angles with fit (green).*

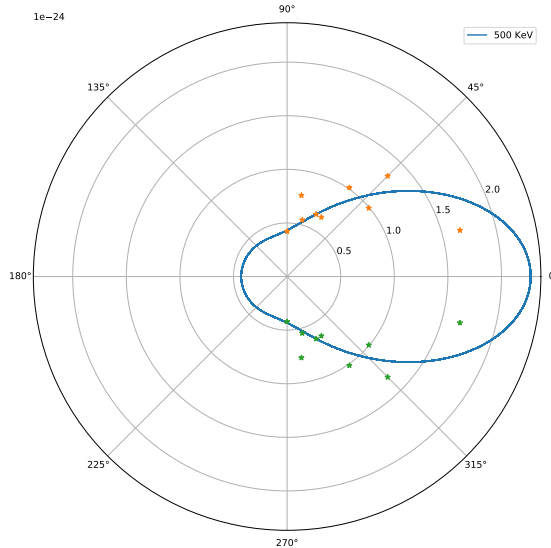


Figure 3.6: *Experimental points and expected shape in polar. The orange points are the actually measured ones, while the green ones are simply their reflection through the x axis of the plane: Klein-Nishina formula is indeed invariant under  $\theta \rightarrow -\theta$ .*

### 3.4 Parity of Positronium

The third and last goal of the experiment, as mentioned in Sec. 1.3, was to verify the theoretical prediction about the parity of the positronium state, which should result to be negative.

Eq. 1.9 shows that for Compton scattering at  $\theta = 90^\circ$ , for photons with orthogonal polarization ( $\phi = 90^\circ$ ) is five times more probable than for the ones with longitudinal polarization. ( $\phi = 0^\circ$ ). So, out of 6 photons detected, 5 are expected to be polarized orthogonally to the scattering plane and only one longitudinally. Implementing two new experimental setups, which are showed in Fig. 3.7, two different measurements can be performed. The first setup is the one represented in the left part of Fig. 3.7: in this case 1" and 2" detectors (respectively the spectrometer and the gate scintillator) detect photons scattered at the same angle ( $\theta = 90^\circ$ ) in the same plane. In the second one (in the right part of Fig. 3.7), instead, 1" detector works in a plane orthogonal to the one of 2" detector.

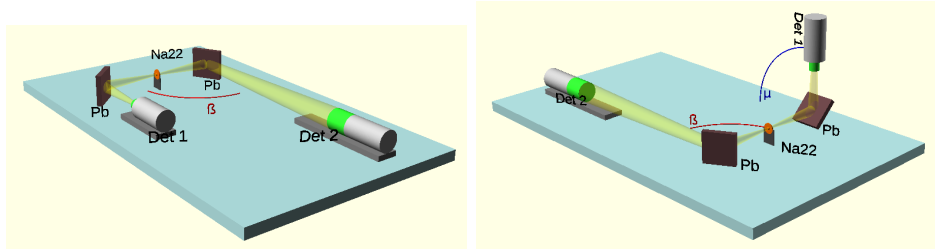


Figure 3.7: *Setup for positronium parity measurements. On the left the detectors are in the same plane while on the right 1" detector works in a plane orthogonal to the one of 2" detector.*

Fig. 3.8 too can be useful for a better comprehension of how the parity of the positronium is related to the polarization of the photons. In the whole image, photons whose polarization vector is drawn in the same colour come from the same decay. Looking at Fig. 3.8.a and Fig. 3.8.b, it can be observed that the polarization vectors of two photons of the same colour are orthogonal to each other. This is the representation of the case in which the positronium, and therefore the annihilation photons, had negative parity (as predicted by Dirac theory). Indeed, the wavefunction for a odd two-photons system is the  $\psi_2$ , previously defined in Eq. 1.7, which has a maximum at  $\alpha=90^\circ$ , i.e. when the photons have relative orthogonal polarization. On the other hand, in Fig. 3.8.c and Fig. 3.8.d photons of the same colour have parallel relative polarization. This would happen if positronium had positive parity, since the wavefunction for an even system of two photons is  $\psi_1$  (defined in Eq. 1.6), which has a maximum at  $\alpha = 0^\circ$ .

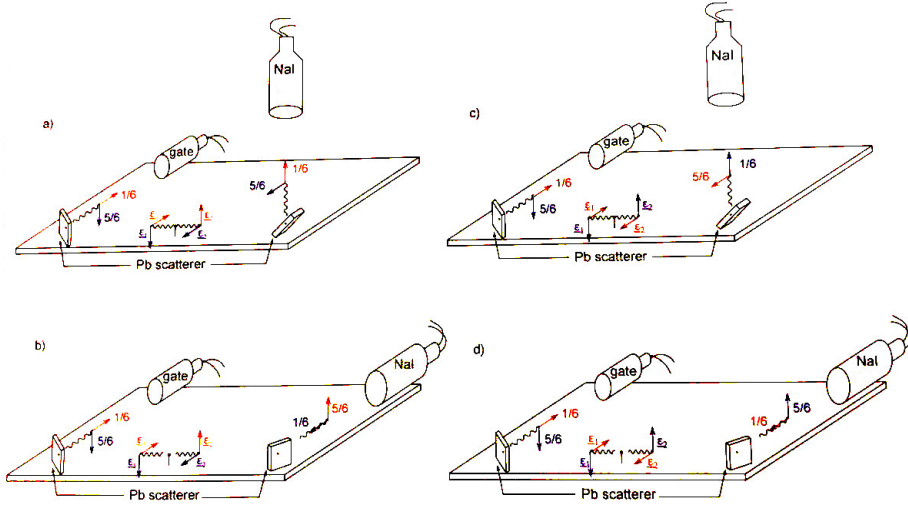


Figure 3.8: *Setup scheme with focus on photons polarization. Photons whose polarization vector is drawn in the same colour come from the same decay.*

In the setup in Fig.3.8.a , the joint probability of both the photons being longitudinally polarized (the red ones) is:

$$\left(\frac{1}{6}\right)^2 = \frac{1}{36}$$

since the two scattering probabilities are independent of each other. On the other hand,

$$\left(\frac{5}{6}\right)^2 = \frac{25}{36}$$

is the joint probability of both being orthogonally polarized. So

$$\frac{1}{36} + \frac{25}{36} = \frac{26}{36}$$

is the probability of both the photons having the same polarization. Probability of the two photons having opposite polarization is then the complementary:

$$1 - \frac{26}{36} = \frac{10}{36}$$

So, the expected ratio between the rates in the two configurations is 26/10. If the positronium parity were positive, the expected ratio could be proved to be 10/26.

In order to perform these rate measurements, a recalibration of the TiSCA windows had to be carried out. Indeed, in the previous measurements the gate opened only for those 511 keV photons that were emitted

directly from the source, while for these ones it had to open for  $90^\circ$ -scattered photons, whose energy is (see Eq. 3.2):

$$\frac{511 \text{ keV}}{2 - \cos\theta} = \frac{511 \text{ keV}}{2} \approx 256 \text{ keV}$$

To calibrate the window around the new peak, different ways could be followed:

1. The first option was to halve the voltage that reaches the TiSCA for the 511 keV window, but, this would decrease the voltage of the PMT, worsening the energy resolution (moreover the voltage-energy relationship of the photomultiplier is not linear). Alternatively, a resistor could be inserted in parallel to halve the voltage at the electronics level, but this alternative would not be very precise too.
2. The second possible way was to select the interesting window using the voltage-energy scale of the MCA (obtained in Sec. 2.6) by taking a ROI (Region Of Interest) as wide as the peak at 511 keV, and translate it to the channels corresponding to 256 keV.
3. As a further alternative, one of the spectra collected for the verification of the Compton Law, in the same configuration (reflection at  $90^\circ$ ), could be used, fixing the window equal to its peak width, measured at 2 or 3  $\sigma$ .
4. Finally, since, contrary to the 511 keV case, the channels cut by the window could not be seen by eye instantaneously, because of the low counting rate, the same procedure could be followed, by waiting to achieve a sufficient amount of counts to recognize the peak at 256 keV and then proceeding with the cut.

All these strategies were adopted to set the window. A new spectrum was taken while the other methods were used to verify the correct functioning of the measuring apparatus.

Once completed the preliminary characterization operations, the scattering with the two scintillators working in orthogonal planes was the first implemented measurement: the setup was the one on the left in Fig. 3.7. Unfortunately, just after the start of the measurement, it was noted that the count rate was extremely low, so that it was decided to let it work for three weeks, checking regularly the spectrum, in particular the region of interest selected by the window, in order to verify whether a peak emerges from the background. The positive outcome of the experiment was not actually guaranteed: indeed, with an approximate calculation, the expected number of counts for a three-week measurement resulted to be roughly 40. The full calculation performed to obtain this value is reported in appendix A.6.

The measurement lasted three weeks and the graph in Fig. 3.9 shows the acquisitions taken each week. As seen in Fig. 3.9, the spectrum does not show a peak in the window around 256 keV so it was not possible to measure the number of counts in this range as the background is much higher than the signal.

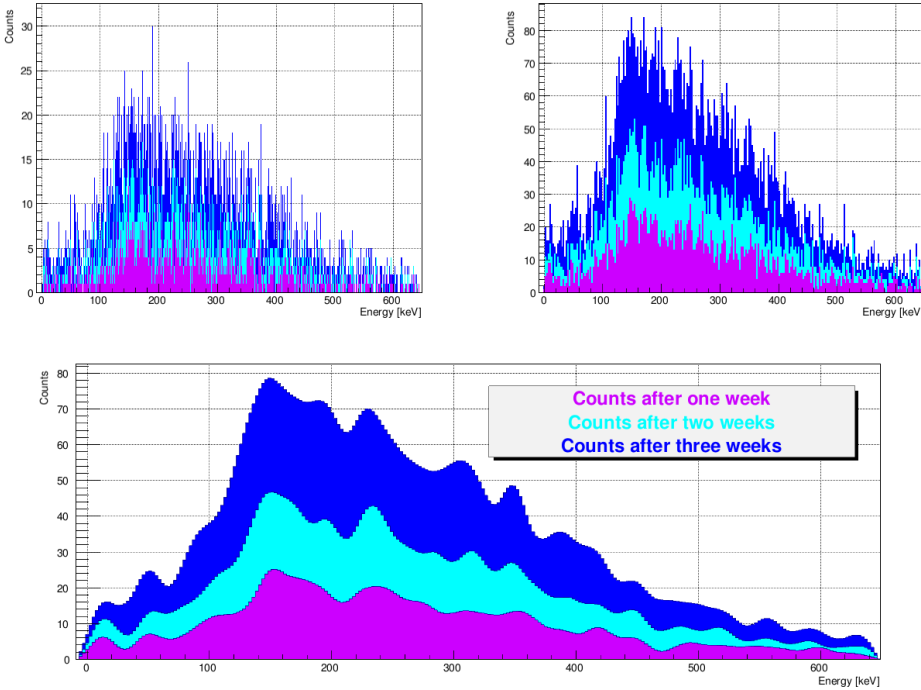


Figure 3.9: *Rebining and smoothing of the spectra taken over the three weeks. Around of 256 keV no measurable peak appears (only from the first to the second week there is a growth above the background while from the second to the third it remains constant.*

From the same graph (Fig. 3.9) is shown how after rebining and smoothing a small peak just below the expected value is obtained. However, in addition to this peak, others also appear that are not due to coincidence and, therefore, it was considered that the best choice was to discard the measurement.

Since no significant signal structure was visible in the spectrum after a measurement time of more than three weeks, it was decided to renounce to study the phenomenology of the positronium decay. The correct setting of the spectral window had been repeatedly verified, so the most probable explanation for the low count rate was that the employed source had an inadequate activity (which value was calculated in Sec. 2.1.1).

Therefore a final measurement was made to verify if the low activity of the source was the reason of the missed goal. This measurement was

performed in exactly the same configuration, but adding three more  $^{22}\text{Na}$  sources (all the ones available in the laboratory), including two significantly more recent than the original one. By doing so, the count rate should be strongly raised and that might allow to understand if this upgrade would be enough to complete the experiment.

Unfortunately, data collection lasted just two days, because of a malfunction in the electrical system of the laboratory.

Indeed, in a three weeks measurement, for the single-source setup, the expected total amount of counts is about 40 (see Appendix. A.6), too few to achieve a sufficiently high signal-to-noise ratio. An estimation of the counts in the window, including the background, gave a rate result of  $8.29e - 04 \text{ Hz}$  while for the setup with four sources, the resulting rate was  $2.36e - 03 \text{ Hz}$ , which is three times greater than the previous one. This indicates that the window was chosen correctly.

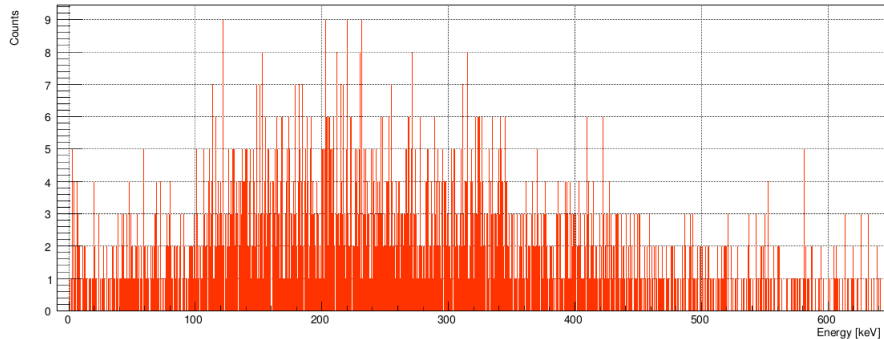


Figure 3.10: Spectrum with four sources of  $^{22}\text{Na}$  lasted two days.

An alternative possible solution was to improve the detection efficiency by reducing the distances between the source, the scatterers and the detectors or by using larger ones, but this would have obviously enlarged the uncertainty on the scattering angle, worsening the resolution and probably preventing the achievement of the goal.

## Chapter 4

# Conclusion

The experience in laboratory with all the measurements lasted one year. It was started with the characterization of the experimental setup described in Cap. 2, mostly regarding the two detectors. After this, the proof of Compton Law and Klein-Nishina formula were successfully performed, contrary, unfortunately, to that of the parity of the positronium.

For what concerns the verification of the Compton Law, results are in line with those expected. It was noted that it is easier for copper to make transmission measurements while for lead it is better to make reflection measurements: this is obviously due to the different ratios between Compton scattering and photoelectric cross section in the materials. In measurements at small angles, a good counting rate was achieved, so that sufficient data were obtained in just a few days. Going up with the scattering angle, measurements of one or two weeks had to be implemented. It was chosen not to take a complete set of data for lead, since the results were the same as for copper despite larger associated errors. These errors are due to the fact that for some of the angles measurements lasted for just a few hours.

For the verification of Klein-Nishina formula, it was decided to use the same data collected for the previous section, using the values of both the efficiency of the two detectors and the activity of the source. Only measurements at angles smaller than  $90^\circ$  were used because they required shorter time to have peaks with a high number of counts. Despite the imperfect obtained cross section values, the estimation of the parameter  $r_0$  (classical electron radius) was quite successful since it was only  $0.44\sigma$  far from the theoretical value.

For the last point of the experiment, however, it was not possible to identify the sought peak, and therefore to verify the theoretical prevision about the positronium parity.

# Appendices

# Appendix A

## Insights

### A.1 Detector 1-inch

In Fig.A.1 the trend of the 1-inch detector resolution for the sodium  $\gamma$  peak (1274 keV) is shown. As it can be seen, the resolution with increasing energy improves reaching 5%. This evidence suggested that the resolution is not constant for the whole spectrum. In fact, since in this experiment the spectrum was measured under the energy of 511 keV, resolution was measured at this energy, and kept constant also in lower energy measures, although it actually worsens with decreasing energy, to provide a wider error band.

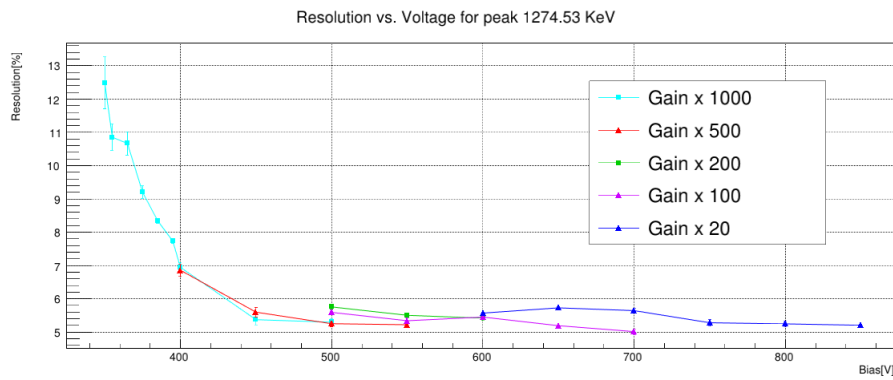
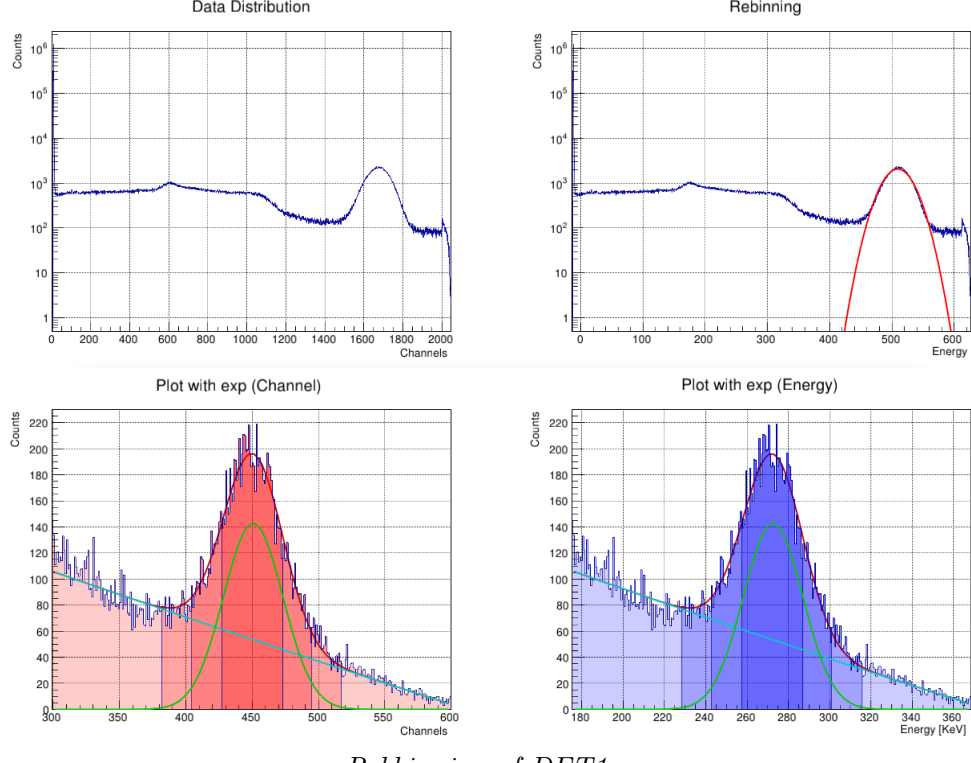


Figure A.1: Resolution DET1 for 1246 KeV.

It is also necessary to consider the error that occurs when a rebin of the measurement scale is carried out by switching from voltage to energy. This error, that in this experiment was considered negligible as it is very small compared to the other ones, is a systematic one. Its source is the fact that the width of the bin (voltage range), which is a finite number as it is digital, has been multiplied by a finite value (eight digits as for double

values) obtained from the calibration to which a bias has been added in order not to associate the energy of 0 keV to the zero channel.



*Rebining of DET1.*

## A.2 Detector 2-inch

The results obtained for the 2-inch detector are reported in the appendix as it was not possible, due to time problems, to perform a "mirror measurement" with respect to the one performed. In fact, an interesting starting point would have been to verify which configuration for the experiment would have been the most suitable. In choosing to use the one-inch detector to perform spectroscopy and the two-inch detector to work as a gate, the subtended solid angles were considered. The detector with a smaller radius would have had the lowest collection efficiency but also the smallest uncertainty on the solid angle and therefore the highest precision on the measurement of energy. However, time was not enough to swap the two detectors and try to use the two-inch one as a spectrometer to observe possible differences. In the initial choice, a response from the two detectors in respect to the supply voltage, resolution and calibration was also reconstructed, as shown in the following graphs (Fig.A.2 and Fig.A.3). This was done precisely because until the last moment the final setup had not yet been chosen.

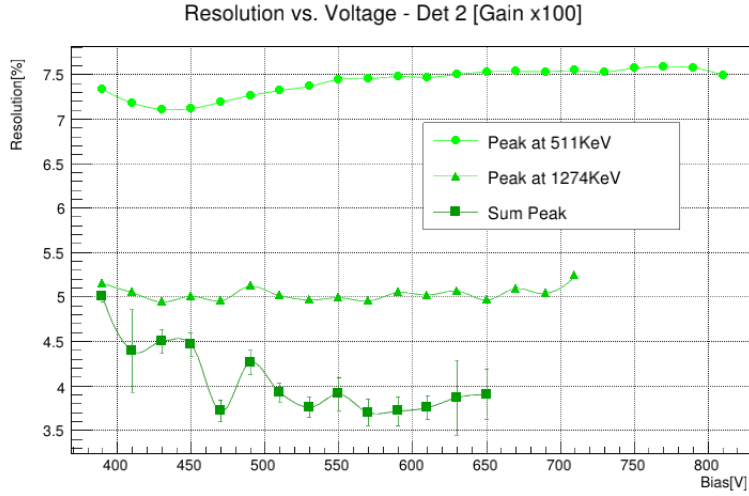


Figure A.2: *Resolution DET2 for different peaks.*

From these values in line with those of the one-inch detector, there is no valid reason to choose *a priori* the two-inch one as the best option for spectroscopy.

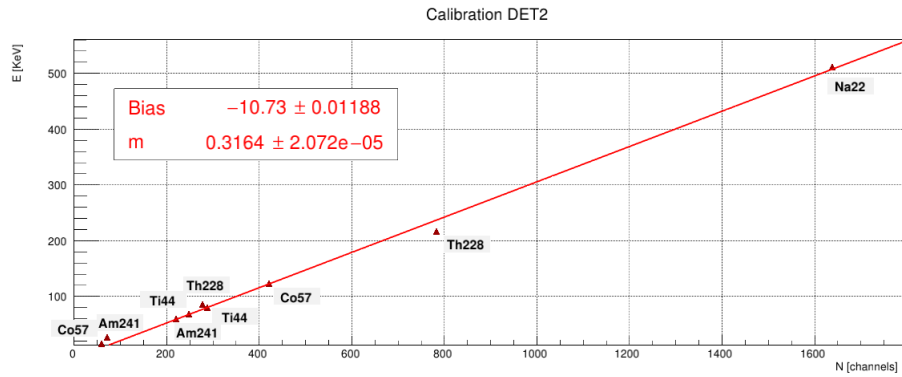


Figure A.3: *Calibration line of the thick detector. Each point corresponds to one peak referred to a specific source.*

The graph of the efficiency of the two-inch detector is also shown below along with the one-inch one in Fig.A.4. Comparing these two graphs we see that as said the efficiency of the largest detector, which is obtained from the parameter  $m$ , the slope of the line, is the best one. However, for both detectors at large solid angles and therefore at short distances from the source, the sampling deviates from the linear fit value. This means that at short distances there is a loss of efficiency if the multiplicative coefficient of  $m$  is considered constant, as it should be.

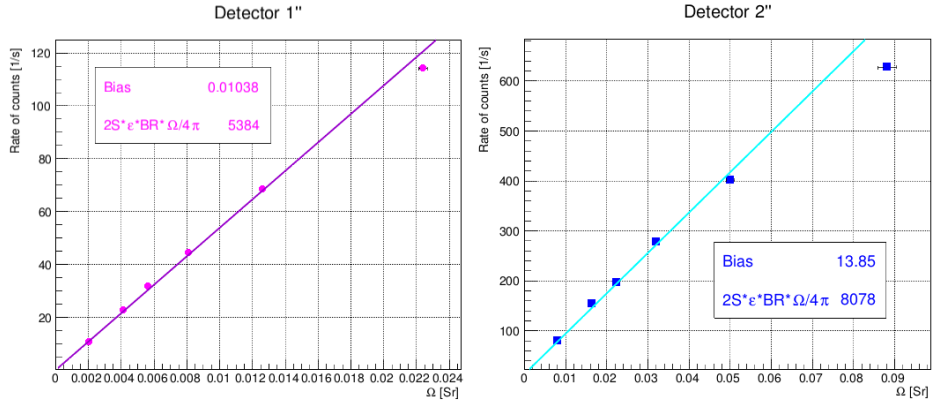


Figure A.4: Comparison between the efficiencies of the two detectors.

### A.3 Smoothing

Since for the Klein-Nishina formula a value constantly lower than the expected one was found, it was tried to increase the counting rate or, equivalently, the number of counts in the peaks collected in a fixed time. An application of the smoothing data technique was therefore tried: a weighted average between the values of each bin, those of the previous one and of the following was performed. Iterating this process several times the gaussian peak takes a "smoother" shape than the original one, (as can be seen in the graphs in Fig.A.5). Assuming a sufficiently solid statistic, this technique also allows to show the presence of structures due to secondary peaks or in general to the background that would otherwise have been confused with the noise or with the poissonian statistic fluctuations to which the content of the bin is subjected. In principle, this technique involves an enlargement of the gaussian shape with a consequent increase in the underlying area. However, it was noted after using this technique that the underlying area does not substantially change, as shown in Tab.A.1. Then it was decided to keep the "raw" data also for those measurements that had the fewest counts, in which the fluctuations are the most relevant.

	$\mu [KeV]$	$\sigma_\mu [KeV]$	$\sigma [KeV]$	$\sigma_\sigma [KeV]$	Counts
No Smooth	280.092	0.273484	14.2924	0.355558	5126.39
Smooth(1)	280.278	0.274144	14.0457	0.350944	4971.04
Smooth(10)	280.304	0.27443	14.0631	0.352238	4973.44
Smooth(500)	280.382	0.272702	13.9798	0.348596	4961.25

Table A.1: Different smoothing plots for the same peak referred to a measurement performed to find the value of the Klein-Nishina cross section.

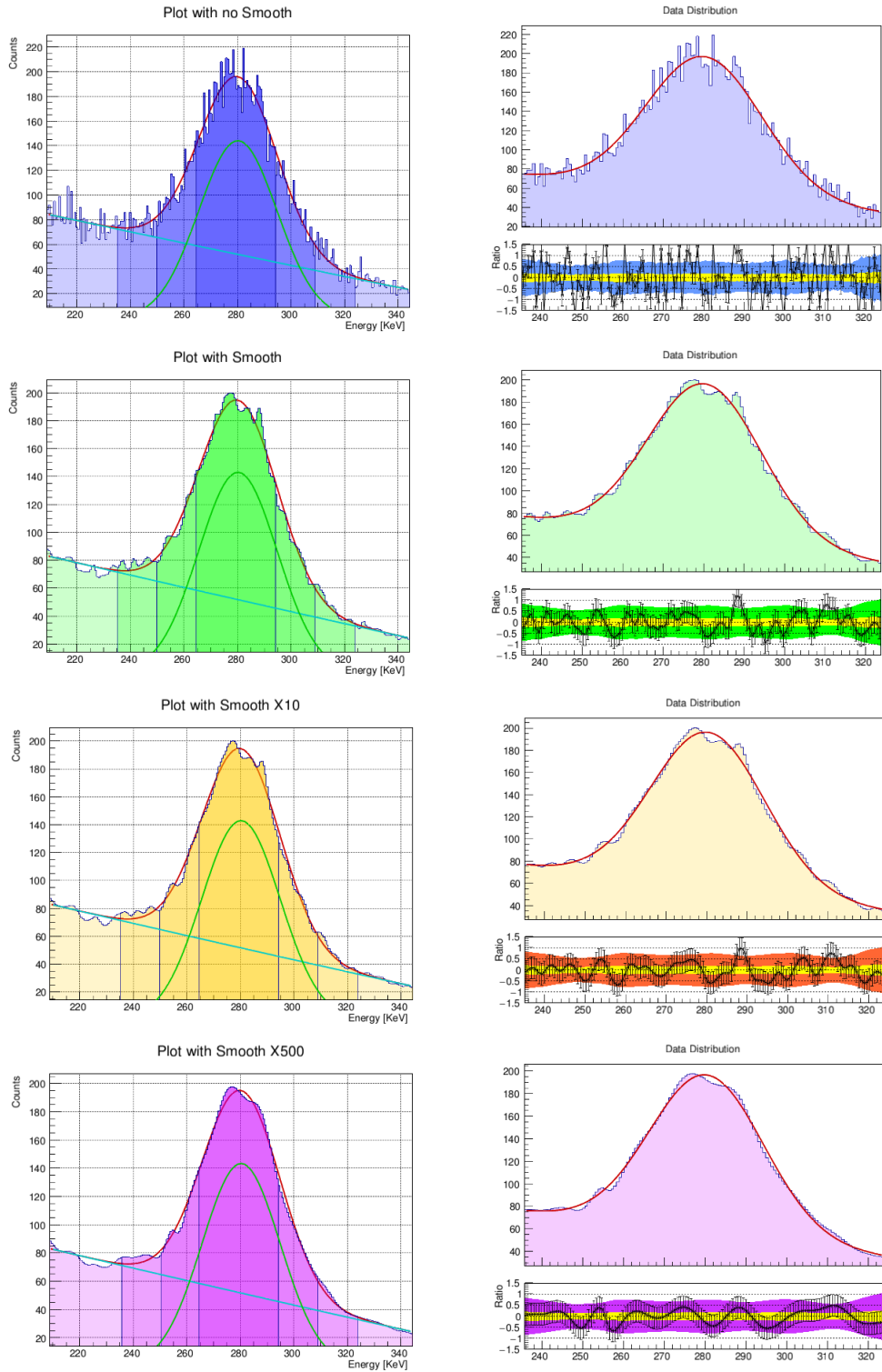


Figure A.5: *Spectrum Smoothing.*

## A.4 Useful Tables

In order to perform the energy calibration of the detector, the characteristic peaks of the used radiation must be correctly identified. Especially for those sources that are in secular equilibrium with the parent and that have therefore an unknown isotopic composition, tables like that in Fig.A.6 were used to recognize the different peaks of the chain.

Radionuclide	Daughter	Energy (keV)	Gamma emissions probability (%)
Ra-228	Ac-228	338.4	11.26
		911.2	26.6
Ra-224	Pb-212	239	43.5
	Bi-212	727.3	6.64
	Tl-208	583.2	30.58
Ra-226	Ra-226	186.2	3.51
	Pb-214	295.2	18.2
		351.9	35.1
	Bi-214	609	44.6
		1,120	14.7

Figure A.6: Table of decay chain of  $^{228}Th$ .

It is also necessary to consider for all the measurements that the presence of other sources in the laboratory, the simple natural radioactivity and the lead shielding could have contaminated the measurement of the source. For this reason we used spectra showing a characteristic background for sodium iodide scintillators and others showing the effect of lead shielding on the detector due to multi-Compton interactions (FigA.7). These spectra were compared with those measured to detect and eliminate all the background peaks.

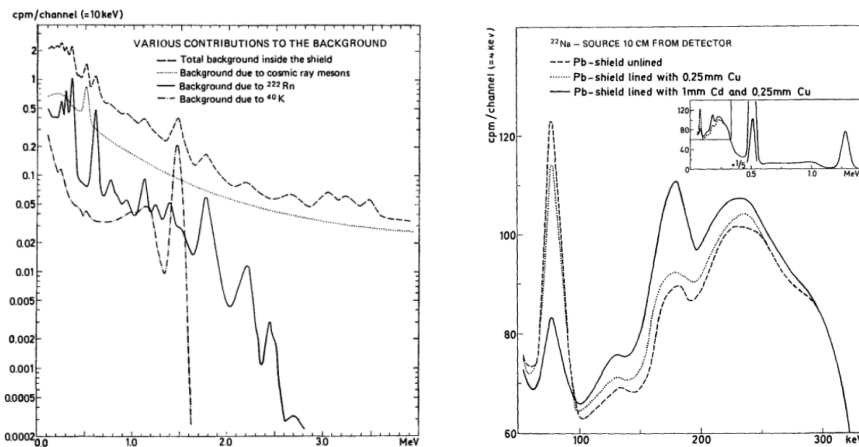


Figure A.7: Natural Background to the left and Background source of a NaI-scintillator shielded with lead to the right.

## A.5 Activity Table

Below is the estimation of the activity value on the days in which the source was used for scattering measurements during the year.

Material		Angle $\theta[^\circ]$	Date[d/m/y]	Activity[kBq]
Copper	<i>Transmission</i>	0	13/01/2021	193.91
		15	05/02/2021	190.55
		30	13/01/2021	193.91
		45	24/02/2021	187.82
		60	08/01/2021	194.65
		75	15/01/2021	193.62
	<i>Reflection</i>	90	20/01/2021	192.88
		10	29/01/2021	191.57
		20	12/02/2021	189.54
		30	03/02/2021	190.84
Lead	<i>Transmission</i>	40	12/02/2021	189.54
		50	18/12/2020	197.78
		55	05/02/2021	190.55
		65	19/02/2021	188.54
	<i>Reflection</i>	80	29/01/2021	191.57
		10	13/02/2021	189.40
		15	24/02/2021	187.82
		20	27/01/2021	191.86
		30	11/12/2020	198.83
		90	09/04/2021	181.65
		120	26/02/2021	187.54

Table A.2: Activity for each measurement with both copper(Cu) and lead(Pb).

## A.6 Rate estimation

In Sec.3.4 an estimation of the expected amount of counts for the measurement in the setup on the left in Fig.3.7 was reported. This calculation was performed to compare the result with the observed one, in order to

understand whether electronics setting problems had occurred.

Since in Sec. 3.4 a counting measurement with two Compton scatterings at  $\theta = 90^\circ$  had to be performed, in this section the joint probability of the two events happening at the same time will be computed, assuming them to be independent of each other.

Solid angles subtended by the targets and the two scintillators are assumed to be all equal, as it roughly was in the experimental setup, to avoid considering geometrical factors of the two detectors, but only the one of the target. From the definition of differential cross section the rate of scattered particles in unit time and solid angle, for a target containing  $N_{e^-}$  electrons, is :

$$\frac{d^2N}{dt d\Omega} = N_{e^-} F \cdot \frac{d\sigma}{d\Omega}$$

and so:

$$\frac{dN}{dt} = N_{e^-} F \cdot \sigma$$

The effective flux  $F$  (*i.e.* keeping in account detectors efficiencies and the attenuation factor of the lead target,  $K_2 \cdot \mu_C$ ) inciding on the target can be expressed as

$$F = 2S \cdot BR \cdot K_2 \cdot \mu_C \frac{\Delta\Omega}{4\pi} \epsilon_1 \epsilon_2 \cdot \frac{1}{\Sigma}$$

where  $\Delta\Omega$  is the solid angle subtended by the target,  $\Sigma$  its surface. :

$$\Delta\Omega \approx \frac{\Sigma}{d^2}$$

( $d$  is the distance between the source and the target)  $K_2 \cdot \mu_C$  for the same target at  $\theta = 90^\circ$  in reflection configuration was computed in Sec.2.10 and was equal to 0.10. For  $\Sigma = 5 \times 5 \text{ cm}^2$ ,  $d = 25 \text{ cm}$ ,  $\epsilon_1 = 0.21$   $\epsilon_2 = 0.16$ ,  $S = 344 \text{ kBq}$ ,  $BR \approx 1$ ,  $F \approx \frac{3Hz}{cm^2}$ . Using Eq.1.5 and Eq.1.1

$$\frac{d\sigma}{d\Omega}(\theta = 90^\circ) = Z \cdot \frac{3}{16} r_0^2$$

and

$$\sigma \approx \frac{d\sigma}{d\Omega} \Delta\Omega \approx Z \cdot 0.04 \cdot \frac{3}{16} r_0^2 \approx 4.87 \cdot 10^{-26} \text{ cm}^2$$

$$N_{e^-} = \frac{Z}{A} \cdot \rho N_A V$$

( $V$  is the volume of the target ( $5 \times 5 \times 0.6 \text{ cm}^3$ )). Computations give:

$$N_{e^-} = 4.05 \cdot 10^{25}$$

and so

$$\frac{dN}{dt} = F\sigma N_{e^-} \approx 0.58 Hz$$

For a three-weeks measurement the total number of  $\theta = 90^\circ$  scatterings expected to occur on the first target is:

$$N_{scatt} = \frac{dN}{dt} \cdot 3 \cdot 7 \cdot 24 \cdot 3600s \approx 1.05 \cdot 10^6$$

So probability  $P$  of Compton scattering at  $\theta = 90^\circ$  is the ratio of the scattered photons  $N_{scatt}$  over the total amount of emitted photons  $N_{tot}$ :

$$P = \frac{N_{scatt}}{N_{tot}} = \frac{1.05 \cdot 10^7}{2S \cdot BR \cdot 3 \cdot 7 \cdot 24 \cdot 3600s} \approx 0.84 \cdot 10^{-6}$$

Therefore the joint probability for two detectable  $\theta = 90^\circ$  scatterings (assuming all the setup precisely equivalent) is  $P_J = P^2 \approx 0.7 \cdot 10^{-12}$ . So the expected amount of counts results to be the number of back-to-back photons pairs times the joint probability:

$$N_{counts} = \frac{N_{TOT}}{2} \cdot P^2 \approx 44$$

# Appendix B

## Instrumentation List

Electronics:

- ORTEC Amplifier, mod. 570
- CAEN 2channel HV programmable power supply, mod. N1470AL
- ORTEC AMP-TSCA, mod. 551
- CAEN Model 93B Dual Timer
- CAEN Model89 Adapter
- Tektronix Mixed Signal Oscilloscope, mod. MSO 2012
- TRUMP-PCI-8K Multichannel Buffer Card

Detectors:

- Pre-Amplifier, mod. 276
- Photomultiplier 905-1 Ortec
- Photomultiplier 905-3 Ortec
- 1-inch NaI(Tl) Scintillator,
- 2-inch NaI(Tl) Scintillator,

Software:

- MAESTRO-32 Mca Emulator
- ROOT Data Analysis Framework ver. 6.22.06

Source:

- Nucl. Na-22, Nominal Activity 367.040 kBq, item 71

# Bibliography

[Pantieri-Gordini, 2012] L.Pantieri, T.Gordini, (2012) *L'arte di scrivere con LaTeX* capitolo 7.2

- [1] G. F. Knoll, *Radiation Detection and Measurement*, Wiley, 4th Edition
- [2] A. Alessandrello, B. Gervasio, L. Zanotti, D. Belluzzo (\*) e S. Donati Guerrieri (\*), *Misura della diffusione Compton in un esperimento a scopo didattico*, Giornale di Fisica, Vol. XXXV n.3, Luglio-Settembre 1994
- [3] National Institute of Standards and Technology (NIST) XCOM, *Element/Compound/Mixture Selection* <https://physics.nist.gov/PhysRefData/Xcom/html/xcom1.html>
- [4] Compton Scattering Experiment, [www.orte](http://www.orte.it)
- [5] Calà, Fiori, Zuccalà, *Compton Scattering Spectroscopy*, 2018-2019